



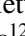
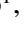








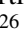







# EWOCs-I: The catalog of X-ray sources in Westerlund 1 from the Extended Westerlund 1 and 2 Open Clusters Survey<sup>★</sup>

M. G. Guarcello<sup>1</sup> , E. Flaccomio<sup>1</sup> , J. F. Albacete-Colombo<sup>2</sup>, V. Almendros-Abad<sup>1</sup> , K. Anastasopoulou<sup>1</sup> , M. Andersen<sup>4</sup>, C. Argiroffi<sup>1,5</sup>, A. Bayo<sup>4</sup> , E. S. Bartlett<sup>4</sup>, N. Bastian<sup>6,7,8</sup>, M. De Becker<sup>9</sup> , W. Best<sup>36</sup> , R. Bonito<sup>1</sup>, A. Borghese<sup>10,11</sup> , D. Calzetti<sup>33</sup>, R. Castellanos<sup>12</sup> , C. Cecchi-Pestellini<sup>1</sup>, J. S. Clark<sup>13,†</sup>, C. J. Clarke<sup>14</sup>, F. Coti Zelati<sup>15,16</sup> , F. Damiani<sup>1</sup>, J. J. Drake<sup>17</sup> , M. Gennaro<sup>26,35</sup> , A. Ginsburg<sup>18</sup>, E. K. Grebel<sup>39</sup>, J. L. Hora<sup>17</sup> , G. L. Israel<sup>19</sup>, G. Lawrence<sup>37,38</sup> , D. Locci<sup>1</sup>, M. Mapelli<sup>20,21</sup>, J. R. Martinez-Galarza<sup>17</sup>, G. Micela<sup>1</sup>, M. Miceli<sup>1,5</sup>, E. Moraux<sup>22</sup>, K. Muzic<sup>3</sup>, F. Najarro<sup>12</sup>, I. Negueruela<sup>23</sup> , A. Nota<sup>26</sup>, C. Pallanca<sup>24,25</sup>, L. Prisinzano<sup>1</sup> , B. Ritchie<sup>13</sup> , M. Robberto<sup>26,32</sup>, T. Rom<sup>22,31</sup> , E. Sabbi<sup>26</sup>, A. Scholz<sup>27</sup>, S. Sciortino<sup>1</sup>, C. Trigilio<sup>28</sup> , G. Umana<sup>28</sup>, A. Winter<sup>29</sup>, N. J. Wright<sup>30</sup>, and P. Zeidler<sup>34</sup> 

(Affiliations can be found after the references)

Received 22 August 2023 / Accepted 21 November 2023

## ABSTRACT

**Context.** With a mass exceeding several  $10^4 M_{\odot}$  and a rich and dense population of massive stars, supermassive young star clusters represent the most massive star-forming environment that is dominated by the feedback from massive stars and gravitational interactions among stars.

**Aims.** In this paper we present the Extended Westerlund 1 and 2 Open Clusters Survey (EWOCs) project, which aims to investigate the influence of the starburst environment on the formation of stars and planets, and on the evolution of both low and high mass stars. The primary targets of this project are Westerlund 1 and 2, the closest supermassive star clusters to the Sun.

**Methods.** The project is based primarily on recent observations conducted with the *Chandra* and JWST observatories. Specifically, the *Chandra* survey of Westerlund 1 consists of 36 new ACIS-I observations, nearly co-pointed, for a total exposure time of 1 Msec. Additionally, we included 8 archival *Chandra*/ACIS-S observations. This paper presents the resulting catalog of X-ray sources within and around Westerlund 1. Sources were detected by combining various existing methods, and photon extraction and source validation were carried out using the ACIS-Extract software.

**Results.** The EWOCs X-ray catalog comprises 5963 validated sources out of the 9420 initially provided to ACIS-Extract, reaching a photon flux threshold of approximately  $2 \times 10^{-8}$  photons  $\text{cm}^{-2} \text{s}^{-1}$ . The X-ray sources exhibit a highly concentrated spatial distribution, with 1075 sources located within the central 1 arcmin. We have successfully detected X-ray emissions from 126 out of the 166 known massive stars of the cluster, and we have collected over 71 000 photons from the magnetar CXO J164710.20-455217.

**Key words.** stars: formation – stars: low-mass – stars: massive – stars: Wolf-Rayet – X-rays: stars – open clusters and associations: individual: Westerlund 1

## 1. Introduction

The star formation rate and the properties of the most common star-forming environments in galaxies vary over time. When considering cosmological timescales, the star formation rate is known to reach its peak at approximately  $z \sim 2-3$  and then gradually decline (e.g., Hopkins & Beacom 2006; Dunlop 2011; Madau & Dickinson 2014). In the local Universe, mergers play a dominant role in shaping the star formation process in galaxies (Rieke & Rujopakarn 2011) as they influence the overall properties of the interstellar medium. Such interactions happen frequently, and various studies have demonstrated that interacting galaxies undergo periods of intense star formation (e.g., Larson & Tinsley 1978; Smith & Struck 2010) because of the considerable impact interactions have on the stars formation process, for instance from the enhancement of the star cluster formation rate due to close encounters (e.g. in the Magellanic

Clouds) and the ram pressure stripping enhancing star formation (e.g., jellyfish galaxies). Noticeable examples are the nearby interacting galaxies M51 and M82, where we observe extreme star formation taking place in very massive young clusters with masses reaching several times  $10^5 M_{\odot}$  (known as super star clusters; de Grijs et al. 2001, 2003b,a). Generally, these highly massive star clusters constitute the dominant star-forming environments in starburst galaxies and are likely prevalent during the peak era of cosmic star formation (e.g., Figer 2008; Adamo et al. 2020).

In the Milky Way, current estimates of the star forming heavily rely on the methods employed. For example, Robitaille & Whitney (2010) derived a range of  $0.68-1.45 M_{\odot} \text{yr}^{-1}$  based on the population of young stellar objects identified in the *Spitzer*/IRAC survey of the Galactic plane GLIMPSE (Benjamin et al. 2003). On the other hand, Licquia & Newman (2015) applied a hierarchical Bayesian statistical method to previous analyses and determined a star formation rate of about  $1.6 M_{\odot} \text{yr}^{-1}$ . For comparison, recent estimates of the star formation rate in M51 range from  $4.8 M_{\odot} \text{yr}^{-1}$  (from a  $158 \mu\text{m}$  map of the galaxy; Pineda et al. 2018) to  $2.7 M_{\odot} \text{yr}^{-1}$  (from combined

<sup>★</sup> Full Table A.1 is available at the CDS via anonymous ftp to [cdsarc.cds.unistra.fr](https://cdsarc.cds.unistra.fr) (130.79.128.5) or via <https://cdsarc.cds.unistra.fr/viz-bin/cat/J/A+A/682/A49>

<sup>†</sup> Deceased.

UV+optical spectral energy distribution fitting; Eufrazio et al. 2017), while in M82 star formation rates of  $2\text{--}4 M_{\odot} \text{yr}^{-1}$  were observed (de Grijs et al. 2001). Nevertheless, all these studies indicate that our Galaxy does not currently have a high star formation rate. Consequently, it is not surprising that the Milky Way lacks a prominent population of super star clusters with masses exceeding  $10^4 M_{\odot}$ . In order of distance from the Sun, the most massive clusters known are Westerlund 1 (2.6–5 kpc; Aghakhanloo et al. 2020; Clark et al. 2005), Westerlund 2 ( $\sim 4.2$  kpc; Vargas Álvarez et al. 2013), NGC 3603 (7.6 kpc; Melena et al. 2008), the Arches and Quintuplet clusters (both at  $\sim 8.5$  kpc; Figer et al. 2002, 1999), Mercer 81 (11 kpc; Davies et al. 2012), and Mercer 30 (12 kpc; de la Fuente et al. 2016). Similar regions in terms of mass, but with a low stellar density, are the Cygnus OB2 association (1.4 kpc; Rygl et al. 2012) and the W3 complex (about 2 kpc; Hachisuka et al. 2006). Slightly older supermassive star clusters (10–20 Myr) are found in the Scutum-Crux arm (about 6 kpc from the Sun; Figer et al. 2006; Davies et al. 2007; Clark et al. 2009). Despite their limited number, these super star clusters hold significant importance as they enable the study of star and planet formation, as well as early stellar evolution, in a star-forming environment that was characteristic of epochs when the Milky Way had higher rates of star formation than today and most of the field stars in our Galaxy formed.

In this paper we present the Extended Westerlund 1 and 2 Open Clusters Survey (EWOCS) project, which is focused on studying star and planet formation and early stellar evolution in compact starbursts, using Westerlund 1 and 2 as first science cases. In particular, this paper focuses on the catalog of X-ray sources detected in the deep *Chandra* observations of Westerlund 1. The paper is organized as follows: we present Westerlund 1 and the EWOCS project in Sect. 2. The EWOCS observations are described in Sect. 3, the procedure for source detection is described in Sect. 4 and that of source validation and extraction in Sect. 5. The final catalog of the X-ray sources in Westerlund 1 is described in Sect. 6.

## 2. Westerlund 1 and the EWOCS project

Westerlund 1 is located at  $RA_{J2000}=16\text{h}47\text{m}04\text{s}$  and  $Dec_{J2000}=-45^{\circ}51'05''$ , corresponding to Galactic coordinates  $l=339.55^{\circ}$  and  $b=-00.40^{\circ}$ . The cluster was discovered by Westerlund (1961) through observations made with the 26-inch Uppsala-Schmidt telescope at Mt. Stromlo Observatory in Australia. From these initial observations, it became evident that Westerlund 1 is a very massive cluster. Today, it is considered to be the most massive young cluster known within the Milky Way, with mass estimates ranging from approximately  $5 \times 10^4 M_{\odot}$  to over  $10^5 M_{\odot}$  (Clark et al. 2005; Brandner et al. 2008; Gennaro et al. 2011; Lim et al. 2013; Andersen et al. 2017).

Despite over 60 yr of studies and observations of Westerlund 1, the tension regarding the parameters of this distinctive cluster remains unresolved. This is primarily due to its compact nature and the significant extinction that has long hindered the ability to resolve its low-mass stars.

The distance to the cluster has been a subject of long-standing debate. The initial estimate by Westerlund (1961) was of 1.4 kpc. However, the same authors later presented a more distant estimate of 5 kpc based on photographic observations in the *VRI* bands (Westerlund 1968). The first study utilizing CCD imaging of the cluster (Piatti et al. 1998) reported a distance estimate of

$1.0 \pm 0.4$  kpc. However, this estimate was based on the incorrect assumption that all cluster members were on the main sequence.

Several authors have made distance estimates for Westerlund 1 based on the analysis of its rich population of massive stars. For example, Clark et al. (2005) based their estimate on six yellow hypergiants (YHGs), assuming that these stars have the standard luminosity for this class of objects ( $\log(L/L_{\odot}) \sim 5.7$ ; Smith et al. 2004), and adopting an extinction of  $A_V=11^m$ , resulting in a distance range between 2 kpc and 5.5 kpc. A similar value was found by Crowther et al. (2006) through infrared analysis of WN and WC stars. Koumpia & Bonanos (2012) derived a distance of  $3.7 \pm 0.6$  kpc from the analysis of the dynamics and geometry of the eclipsing binary W13. By comparing the cluster locus in color-magnitude diagrams with suitable isochrones, Brandner et al. (2008) determined a distance of  $3.55 \pm 0.17$  kpc, while Gennaro et al. (2011) found a distance of  $4.0 \pm 0.2$  kpc, and Lim et al. (2013) reported a distance of about 3.8 kpc. An independent estimate ( $3.9 \pm 0.7$  kpc) was provided by Kothes & Dougherty (2007) using the radial velocity of HI clouds in the direction of the cluster, assuming they were physically connected to Westerlund 1.

More recently, *Gaia* data have been extensively utilized to measure the distances of star clusters, providing precise values up to distances of about 1 kpc (Gaia Collaboration 2016). However, for more distant clusters, careful analysis and assumptions are required to obtain reliable distance measurements. Consequently, it is not surprising that different estimates of the distance to Westerlund 1 have emerged from authors who have analyzed *Gaia* data. Aghakhanloo et al. (2020) conducted a Bayesian analysis of *Gaia* data along the line of sight to Westerlund 1 and obtained a mean cluster parallax of  $0.35^{+0.07}_{-0.06}$  mas, which corresponds to a distance of  $2.6^{+0.6}_{-0.4}$  kpc and is in tension with the previous estimate of approximately 0.19 mas provided by Clark et al. (2020). Focusing on known members of Westerlund 1, Davies & Beasor (2019) found a distance of  $3.9^{+1.0}_{-0.64}$  kpc. More recently, Negueruela et al. (2022) carried out a detailed determination of candidate members in Westerlund 1 using *Gaia* Early Third Data Release (EDR3; van Leeuwen et al. 2021) data and obtained a distance of  $4.23^{+0.23}_{-0.21}$  kpc, suggesting that the cluster is located in the Norma arm. A similar estimate from the *Gaia*/EDR3 was obtained by Navarete et al. (2022).

Given the uncertainty surrounding the distance to Westerlund 1, it is not surprising that estimates of the cluster's age provided by different authors also vary significantly. Age estimates in the range of 3.2 to 5 million years have been derived using isochrone fitting on the high-mass sequence and arguments based on the diverse population of massive stars, including Wolf-Rayet (WR) stars, YHGs, and red supergiants (RSGs; Clark et al. 2005; Crowther et al. 2006; Brandner et al. 2008; Ritchie et al. 2010; Gennaro et al. 2011; Koumpia & Bonanos 2012; Kudryavtseva et al. 2012; Mackey et al. 2015). These authors found a relatively narrow age spread, with an upper limit of 0.4 million yr indicating that Westerlund 1 likely formed in a single burst of star formation (Kudryavtseva et al. 2012). However, some of these estimates are based on arguments that strictly apply to single stars, whereas it is known that the binary fraction among the massive members of Westerlund 1 is very high (Crowther et al. 2006). More recent studies suggest a more complex star formation history and a slightly older age (Aghakhanloo et al. 2020; Beasor et al. 2021; Navarete et al. 2022; Negueruela et al. 2022). In particular, arguments based on spectral energy distribution fitting and the luminosity of individual RSGs support an age estimate exceeding 10 Myrs

(Beasor et al. 2021; Navarete et al. 2022), although this estimate is in tension with other properties of the cluster.

There is a general consensus in the literature regarding other important properties of Westerlund 1, including its high extinction, large mass, and notably, its impressive population of massive stars. The significant extinction toward Westerlund 1 has been acknowledged since the initial publication on this cluster, where an approximate visual extinction of  $A_V \sim 12^m$  has been found (Westerlund 1961). Subsequent estimates range from  $10^m$  to  $13^m$  of visual extinction (Negueruela et al. 2010; Lim et al. 2013; Damineli et al. 2016). There is some disagreement regarding the extinction law in the direction of Westerlund 1: while according to Negueruela et al. (2010) it follows the standard law in the *VRI* bands, Lim et al. (2013) and Damineli et al. (2016) suggested a steeper extinction law in the near-IR ( $R_V = 2.50 \pm 0.04$ ).

The most remarkable characteristic of Westerlund 1 is its large population of massive stars (Clark et al. 2005, 2020; Ritchie et al. 2009), which includes 24 WR stars (Clark & Negueruela 2002; Negueruela & Clark 2005; Skinner et al. 2006; Groh et al. 2006; Crowther et al. 2006), the luminous blue variable (LBV) Wd1-243 (Clark & Negueruela 2004), ten YHG with spectral classes ranging from A5Ia<sup>+</sup> to F8Ia<sup>+</sup> (Clark et al. 2005)<sup>1</sup>, two blue stragglers (Clark et al. 2019), four RSGs (Wright et al. 2014b), seven blue hypergiants (BHGs), and over 100 bright OB supergiants dominated by spectral classes O9-B1 (Negueruela et al. 2010). Most of these sources are concentrated in the inner region of the cluster, spanning approximately 1 arcmin, with only a few more isolated massive stars, such as WR77.

In particular, Westerlund 1 hosts examples of every known transitional evolutionary phase between H-rich OB supergiants and H-depleted WR stars. This makes the cluster a unique target for studying massive stars and, specifically, for understanding how binarity and mass loss impact the evolutionary paths of these stars and how the initial stellar masses are linked to the types of compact objects that form at the end of their evolution. Winds and mass loss in these stars have been extensively studied with radio and millimeter-continuum observations, which have detected individual bright sources, such as W9, surrounded by extended nebulae, providing evidence of intense mass loss in the past (up to several  $10^{-4} M_\odot$  per year, Dougherty et al. 2010; Fenech et al. 2018; Andrews et al. 2019). These short-lived and episodic mass-loss events appear to be necessary to explain the diversity of evolved massive stars in Westerlund 1.

Westerlund 1 is rich in binary systems. A high binary fraction has been identified in massive stars through spectroscopic (Ritchie et al. 2022), radio (Dougherty et al. 2010), infrared (Crowther et al. 2006), and X-ray (Skinner et al. 2006; Clark et al. 2008, 2019) observations. For instance, the WR population of Westerlund 1 has an estimated binary fraction of at least 70% (Crowther et al. 2006; Clark et al. 2008). Isolated stars are primarily found among the mid-B to F hypergiants, with the exception of the LBV star W243, whose binarity is supported by interferometric (Clark et al. 2019), X-ray (Mahy et al. 2022), and spectroscopic (Ritchie et al. 2009) observations.

This harsh environment is expected to have effects on the star formation process, the evolution and dispersal of protoplanetary disks, and the formation and early evolution of planets and their atmospheres. While no studies to date have been able to

identify the population of protoplanetary disks in Westerlund 1 and explore the feedback provided by the starburst environment on their evolution and dispersal, several authors have attempted to quantify the cluster's initial mass function (IMF) to investigate possible deviations from the universal law. An IMF consistent with the Salpeter (1955) law has been found by Brandner et al. (2008) in the  $3.4\text{--}27 M_\odot$  range, by Gennaro et al. (2011) extrapolated in the  $0.5\text{--}120 M_\odot$  range, and Andersen et al. (2017) down to  $0.15 M_\odot$  in the outer cluster, while a shallower IMF slope was found by Lim et al. (2013), integrated in the  $0.08\text{--}85 M_\odot$  range.

### 2.1. Previous X-ray observations

X-ray observations of young clusters provide valuable diagnostics for selecting pre-main-sequence (PMS) stars independently of the presence of circumstellar disks (e.g., Montmerle 1996), down to low stellar masses (e.g., Getman et al. 2005; Barrado et al. 2011). Additionally, in a cluster rich in massive stars with a very compact configuration, X-ray observations can reveal a plethora of processes and physical mechanisms that play an important role in the evolution of massive stars (Seward et al. 1979; Berghoefter et al. 1996). It is also worth mentioning that only the *Chandra* X-Ray Observatory (Weisskopf et al. 2002) can currently provide the high spatial resolution required to resolve individual X-ray faint sources in a crowded cluster like Westerlund 1. Given the designs of future X-ray missions currently in development, such observations will likely be challenging for quite some time after the *Chandra* era.

Both *Chandra* and XMM have been used in the past to observe Westerlund 1. The initial observations performed with *Chandra* reached a depth of approximately 58 ksec (P.I. Skinner) and resolved numerous X-ray sources (Skinner et al. 2006; Munro et al. 2006; Clark et al. 2008). Skinner et al. (2006) focused on the WR stars and their spectral properties, detecting 12 out of 24 known stars and finding strong evidence for the existence of very hot plasma in the circumstellar environment in the two brightest objects (W72/A and WRB), strongly suggesting the presence of a colliding winds in these binary systems; Munro et al. (2006) studied the diffuse X-ray emission and its dominating hard spectral component, which was later confirmed by Kavanagh et al. (2011) from 48 ks *XMM-Newton* observations. These authors detected a strong Fe 6.7 keV line in the diffuse emission spectrum, indicating its thermal nature. Clark et al. (2008) found that 46 known high-mass members of Westerlund 1 were detected in X-rays, and they supposed that the remaining  $\sim 60$  X-ray sources detected in these images are likely PMS stars with masses  $\leq 1.5 M_\odot$ .

Since its discovery by Munro et al. (2006), the magnetar CXO J164710.2-455216 (CXOU J16) in Westerlund 1 — the brightest X-ray source in the cluster — has garnered significant attention. Dedicated observations using *XMM-Newton* and *Chandra*/ACIS-S have accumulated a total exposure of 273.14 ksec (P.I.s Israel, Munro and Scharrel) and 94.65 ksec (P.I.s Israel and Rea), respectively. A typical property of this class of pulsars is their frequent bursts and recurrent outbursts. In fact, three distinct outbursts from CXOU J16 have been observed in the past 17 yr (Borghese et al. 2019). The first one occurred in September 2006 and was triggered by a short burst that released an energy of approximately  $10^{39}$  erg in the 15–150 keV band (Krimm et al. 2006). It was followed by a second outburst in September 2011 (Israel et al. 2011), during which the pulsar exhibited a peculiar behavior: the pulse profile evolved from a single peak in the pre-outburst phase to an energy-dependent tri-peaked profile post-outburst. The overall spectrum evolved from a single blackbody to a more complex shape that was well

<sup>1</sup> A different classification for six YHG has recently been presented by Beasor et al. (2023).



modeled by including an additional hotter blackbody component. The most recent outburst was again triggered by a short burst detected by the *Swift* Burst Alert Telescope in May 2017 (D’Ai et al. 2017). During these intense outburst activities, the magnetic field strength was estimated to range from  $7 \times 10^{13}$  G (a value typical for low-field magnetars, Perna & Pons 2011) to  $\sim 10^{14}$  G (An et al. 2013; Israel et al. 2007).

## 2.2. The EWOCs project

The pre-EWOCs *Chandra* observations of Westerlund 1 have been analyzed by Townsley et al. (2018) in the framework of the Second Installment of the Massive Star-forming Regions Omnibus X-ray Catalog (MOXC2), identifying 1721 X-ray sources. This work has confirmed that Westerlund 1 is rich in X-ray bright sources, even though its low-mass stellar content remained undetected in the pre-EWOCs observations. According to these authors, the X-ray luminosity limit in the broad band where half of the brighter population is detected was  $\log(L_x) = 30.69$ , with  $L_x$  in  $\text{erg s}^{-1}$ , corresponding to a  $1.5 M_\odot$  star<sup>2</sup>.

The need to unveil the low-mass population of Westerlund 1 has motivated the 1 Msec observation of Westerlund 1 (P.I. Guarcello) with the *Chandra* Advanced CCD Imaging Spectrometer (ACIS-I; Garmire et al. 2003), which, together with a 18.9 h Cycle 1 JWST/MIRI and NIRCам observation (program ID 1905, P.I. Guarcello) and a 48 ksec NICER observation (P.I. Borghese) of CXOU J16, constitutes the set of new observations of the EWOCs project<sup>3</sup>. The main objective of EWOCs is to use Westerlund 1 and 2 as a test cases for understanding how star and planet formation, early stellar evolution, and the production of compact objects occur in a starburst environment. Specifically, the project aims to achieve the following objectives:

- Unveil the low-mass stellar population of Westerlund 1 and 2, both in their core and halo. X-ray observations are expected to be critically important for selecting cluster members in the halo, where contamination from background and foreground sources could affect membership determination based on photometric data.
- Determine the actual stellar content of the clusters, down to the low-mass regime, mainly thanks to the JWST observations; calculate their IMF down to the brown dwarf regime, and understand whether the starburst environment impact the formation of low-mass and very-low mass stars.
- Study the clusters properties, particularly age, age spread, morphology and dynamics. The project aims to understand whether the clusters formed in a single burst of star formation or through a process spanning several million years, as well as how and if they will disperse.
- Identify the disk-bearing population of the clusters, mainly through the JWST observations. Combining this with the detection of disk-less stars from the *Chandra*/ACIS-I observations and modeling of disks dispersal, we will finally assess how disks evolve and how planet formation proceeds in a starburst environment.
- If planets can form, understand how they evolve while immersed in such an environment characterized by high local fluxes of UV and X-ray radiation and relativistic particles.

<sup>2</sup> As stated by Townsley et al. (2018), the corresponding X-ray flux has been calculated using PIMMS6 assuming a limit of five-counts detection on-axis, for a source with an APEC thermal plasma with  $kT = 2.7$  keV and abundance  $0.4 Z_\odot$ , which are typical values for a PMS star (Preibisch et al. 2005).

<sup>3</sup> <https://Westerlund1survey.wordpress.com/>

- Study how binarity and mass-loss affect the evolution of the massive stars in the clusters, and how their initial mass is mapped into the type of compact objects formed at the end of their evolution.
- Determine whether binarity across stellar masses is different in a starburst environment.
- Study for the first time the status of CXOU J16 far from bursts, which will allow us to estimate the intrinsic properties of the pulsar.
- Search for the expected population of compact objects that have been suggested to exist in Westerlund 1, since, under specific assumptions, up to  $\sim 65$  core-collapse supernovae could have already occurred in the cluster (Muno et al. 2006; Brandner et al. 2008). Besides, Westerlund 1 is one of the few known star clusters meeting the properties required for the formation of intermediate mass black holes from run-away coalescence (Portegies Zwart et al. 2004). As estimated by Clark et al. (2008), such objects, if present and if currently accreting mass, should be observable with a very deep *Chandra* observation.
- Understanding how stellar winds from massive evolved stars can affect the ISM to produce diffuse X-ray emission, whether this hot gas could affect star formation throughout the region, and whether we can prove ongoing accumulation of polluted material in the cluster core.

Figure 1 shows the contours of the pre-EWOCs and EWOCs observations of Westerlund 1 and CXOU J16, plotted over the combined *Chandra* event file and a  $K_S$  band image of the cluster and the surrounding area obtained with the FourStar infrared camera mounted on the *Magellan* 6.5 m telescopes.

## 3. *Chandra* observations and data reduction

### 3.1. Overview of the *Chandra*/ACIS observations

The EWOCs survey also includes eight pre-EWOCs observations performed with ACIS-S, two of which were pointed at Westerlund 1 and six at CXOU J16. These observations were conducted between June 2005 and February 2018 (Table 1). Additionally, 36 EWOCs observations were carried out with the ACIS-I detector from June 2020 to August 2021. The aim point of each ACIS-I observation was adjusted based on the nominal roll angle, as indicated in Table 2. This adjustment was crucial to for avoiding gaps that cover the cluster core, the pulsar, or some of the brightest massive members, while ensuring the cluster remained within the inner arcminute. By adopting this design, we maximized the benefits of the subarcsecond spatial resolution and sensitivity in the central part of the ACIS-I detector to observe the cluster core, which is highly compact and crowded.

The total exposure for the pre-EWOCs observations is 151.93 ksec, while for the EWOCs observations it is 967.80 ksec. The exposure times for the individual EWOCs observations range from 11.92 ksec (Obs.ID 23272) to 39.55 ksec (Obs.ID 22319), with a mean exposure of 26.33 ksec. The EWOCs observations span over 1 yr, providing a robust baseline for studying the X-ray variability of the brightest sources. All EWOCs observations were conducted using the ACIS-I detector in imaging mode, utilizing all four chips (I0–I3). The observations were performed in the VERY FAINT mode, which employs telemetry in  $5 \times 5$  pixel event islands for improved background suppression<sup>4</sup>. When combined with the pre-EWOCs observations, the

<sup>4</sup> [http://cxc.harvard.edu/cal/Acis/Cal\\_prods/vfbkgrnd/index.html](http://cxc.harvard.edu/cal/Acis/Cal_prods/vfbkgrnd/index.html)

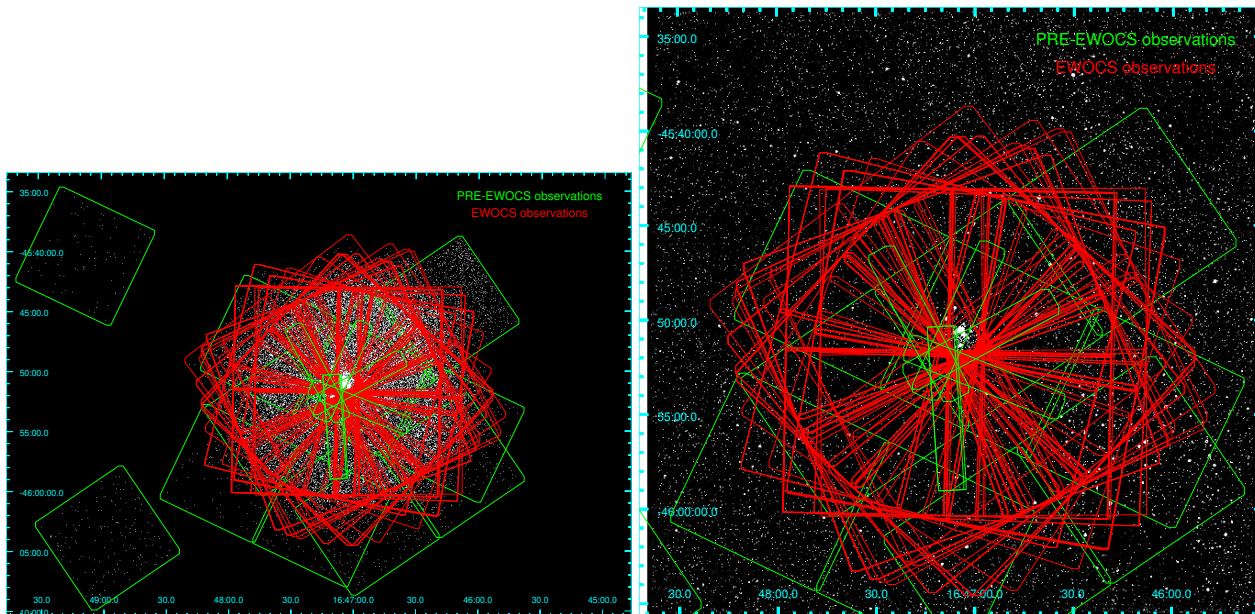


**Fig. 1.** Contours of the pre-EWOCS and EWOCS *Chandra* observations of Westerlund 1 overlaid on the combined ACIS event file (left panel) and on an image in the *Ks* band obtained with the FourStar infrared camera mounted on the *Magellan* 6.5 m telescopes (right panel).

**Table 1.** Pre-EWOCS observations of Westerlund 1.

Obs.ID.	Instrument	Exposure ksec	Roll angle degrees	RA J2000	Dec J2000	Date	P.I.
5411	ACIS-S	38.47	326	16:47:05.40	-45:50:36.70	2005-06-18	Skinner
6283	ACIS-S	18.81	25	16:47:05.40	-45:50:36.70	2005-05-22	Skinner
14360	ACIS-S	19.06	242	16:47:10.20	-45:52:16.90	2011-10-23	Israel
19135	ACIS-S	9.13	22	16:47:10.20	-45:52:17.00	2017-05-25	Rea
19136	ACIS-S	13.67	331	16:47:10.20	-45:52:17.00	2017-06-16	Rea
19137	ACIS-S	18.2	295	16:47:10.20	-45:52:17.00	2017-07-10	Rea
19138	ACIS-S	18.2	86	16:47:10.20	-45:52:17.00	2018-02-24	Rea
20976	ACIS-S	16.39	86	16:47:10.20	-45:52:17.00	2018-02-25	Rea

total time baseline exceeds 16 yr, which is particularly valuable for studying certain sources in the cluster, such as the magnetar. Figure 2 displays a composite RGB ACIS image of Westerlund 1, where colors represent different photon energies (red: soft band, green: medium band, blue: hard band). The image shows both the entire EWOCS field and a central region of approximately  $\sim 3'$ . In the right panel, it is evident that the source density is high in the cluster core and it reveals that the majority of faint sources are predominantly hard, likely due to high absorption or since they have been observed during periods of intense magnetic activity such as flares. The list of *Chandra* datasets used in this paper, and obtained by the *Chandra* X-ray Observatory, are contained in the *Chandra* Data Collection (CDC) 153<sup>5</sup>.

### 3.2. Data reduction

The *Chandra* observations were analyzed using the “pre-ACIS Extract workflow” procedure outlined in Townsley et al. (2003) and Broos et al. (2010). This procedure utilizes various tools integrated within the *Chandra* Interactive Analysis of Observations (CIAO) software (Fruscione et al. 2006). We employed versions 4.13 of CIAO along with the CALDB 4.9.5 calibration files.

<sup>5</sup> <https://doi.org/10.25574/cdc.153>

The L1-to-L2 processing flow aims to generate calibrated *Chandra* event files from the L1 products provided by the *Chandra* X-Ray Center (CXC). It includes event energy calibration, refinement of event positions, and correction for contamination caused by bad pixels and cosmic-ray afterglow. This workflow utilizes a less aggressive bad pixel table compared to the one produced by CIAO and it incorporates the *clean55* algorithm for background reduction. Additionally, cosmic-ray afterglows are removed, and the source point spread function (PSF) is improved by disabling the random  $\pm 0.25$  pixel randomization. The standard grade filter is applied to events, retaining only *ASCA* grades 0, 2, 3, 4, and 6. However, events are not filtered for the standard *status=0* requirement, which may result in the exclusion of a significant number of reliable events.

Afterglows, which are groups of events appearing at the same location in consecutive CCD frames, can often be mistaken for faint sources. To address this, the CIAO tool *acis\_detect\_afterglow* is typically employed to remove afterglows. This tool applies a relatively aggressive cleaning approach, eliminating several false positives. Another tool, *acis\_run\_hotpix*, is less aggressive but it may fail to detect afterglow series with fewer than ten counts. In this L1-to-L2 procedure, a bifurcated workflow is adopted, where we applied an aggressive cleaning to the files used for source detection and

**Table 2.** EWOCs observations.

Obs.ID.	Exposure ksec	Roll angle degrees	RA J2000	Dec J2000	Date
22316	39.55	245	16:46:59.97	-45:51:13.70	2020-10-04
22317	24.75	272	16:47:00.55	-45:51:29.59	2021-08-14
22318	26.72	312	16:47:03.24	-45:51:45.84	2020-06-25
22319	46.45	243	16:46:59.97	-45:51:13.70	2020-10-09
22320	37.58	321	16:47:05.45	-45:51:39.01	2020-06-20
22321	37.58	1	16:47:04.93	-45:51:14.41	2020-06-02
22977	37.57	236	16:46:59.97	-45:51:13.70	2020-10-22
22978	24.75	340	16:47:05.45	-45:51:39.01	2021-06-12
22979	21.79	14	16:47:07.63	-45:51:13.62	2021-05-28
22980	24.75	331	16:47:05.45	-45:51:39.01	2021-06-16
22981	21.85	314	16:47:03.24	-45:51:45.84	2021-06-24
22982	16.85	335	16:47:05.45	-45:51:39.01	2020-06-13
22983	27.72	340	16:47:05.45	-45:51:39.01	2021-06-09
22984	22.61	303	16:47:03.24	-45:51:45.84	2021-07-02
22985	24.75	52	16:47:07.13	-45:50:48.14	2021-05-01
22986	17.67	335	16:47:05.45	-45:51:39.01	2020-06-11
22987	24.75	1	16:47:04.93	-45:51:14.41	2021-06-04
22988	17.85	280	16:47:02.20	-45:51:31.62	2021-07-27
22989	21.79	14	16:47:07.63	-45:51:13.62	2021-05-27
22990	24.75	288	16:47:01.97	-45:51:40.91	2020-07-17
23272	11.92	1	16:47:04.93	-45:51:14.41	2020-06-03
23279	29.69	335	16:47:05.45	-45:51:39.01	2020-06-12
23281	30.49	321	16:47:05.45	-45:51:39.01	2020-06-21
23287	34.61	312	16:47:03.24	-45:51:45.84	2020-06-26
23288	29.18	312	16:47:03.24	-45:51:45.84	2020-06-26
24827	24.75	269	16:47:00.55	-45:51:14.83	2021-08-21
24828	24.75	1	16:47:04.93	-45:51:14.41	2021-06-04
25051	31.66	14	16:47:07.63	-45:51:13.62	2021-05-28
25055	29.68	1	16:47:04.93	-45:51:14.41	2021-06-05
25057	25.25	340	16:47:05.45	-45:51:39.01	2021-06-13
25058	27.22	333	16:47:05.45	-45:51:39.01	2021-06-10
25073	34.62	314	16:47:03.24	-45:51:45.84	2021-06-25
25096	18.14	280	16:47:02.20	-45:51:31.62	2021-07-29
25097	23.59	280	16:47:02.20	-45:51:31.62	2021-07-30
25098	25.43	280	16:47:02.20	-45:51:31.62	2021-08-01
25683	24.74	272	16:47:00.55	-45:51:29.59	2021-08-15

validation, and a less aggressive cleaning for the files used in spectral analysis.

The background light curves were examined to identify and exclude intervals with intense and fluctuating background. This correction was required only for Obs.ID 5411, as the background remained relatively stable throughout the other observations.

The astrometry of the event files was corrected in three steps. In the first step, we addressed the offset of each Obs.ID relative to Obs.ID 22319, which is the deepest observation. We utilized *Wavdetect* to identify the brightest sources in each observation and cross-matched their positions with those detected in the Obs.ID 22319 image. Subsequently, we employed the CIAO tools *wcs\_match* and *wcs\_update* to update the astrometry for each observation. In the second step, which was part of the L1-to-L2 workflow, we corrected the astrometry of each event file using the *Gaia* Third Data Release (DR3; [Gaia Collaboration 2023](#)) astrometric system. This process was repeated as the third step, but using the brightest sources from the final list of validated sources (Sect. 6).

Exposure maps were calculated using the standard CIAO tools implemented in the pre-ACIS Extract workflow for each observation in the broad (0.5–7.9 keV), soft (0.5–1.0 keV), medium (1.0–2.0 keV), hard (2.0–7.9 keV), and very hard (4.0–7.9 keV) bands, and subsequently combined. The resulting combined exposure map in the broad band is displayed in Fig. 3, revealing a deep and nearly uniform exposure in the central region. This region is sufficiently large to encompass both the core of Westerlund 1 and a portion of the expected halo of the cluster (as recently discovered, extended haloes are typically associated with stellar clusters; [Meingast et al. 2021](#); [Prisinzano et al. 2022](#)).

#### 4. Source detection

The strategy we employed for source detection aims to maximize the depth of the EWOCs catalog, even in the core of Westerlund 1. This region presents challenges due to source confusion and a bright, irregular background, making the detection of faint sources a complex task (see Fig. 4).



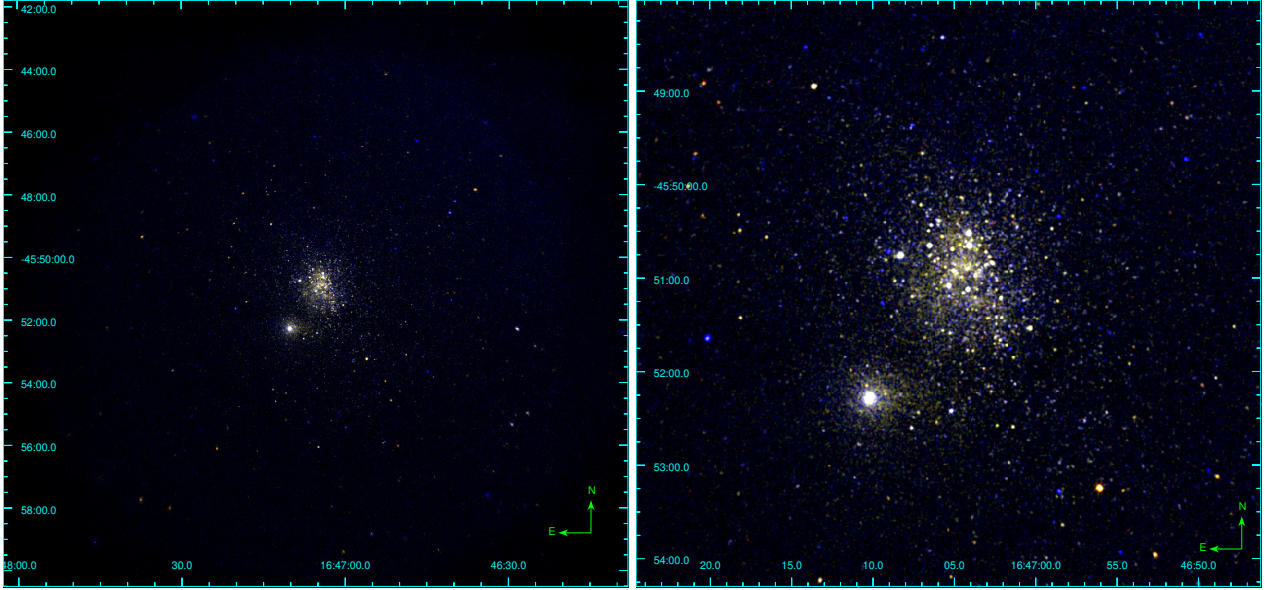


**Fig. 2.** RGB images of the whole ACIS-I field (left panel) and the central area (right panel) of the composite *Chandra* images. Soft band (0.5–1.0 keV) photons are marked in red, medium band (1.0–2.0 keV) photons in green, and hard band (2–7.9 keV) photons in blue. The brightest source in the southeast direction is CXOU J16. The two images were smoothed adopting a Gaussian kernel with a radius of 2 pixels.

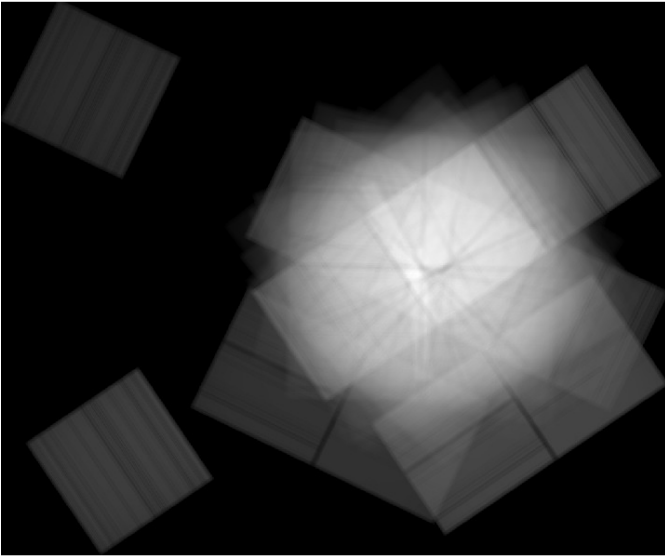


**Fig. 3.** Combined exposure map in the broad band.

Source detection is implemented using four different methods:

- The wavelet-based algorithm *PWDetect* (Damiani et al. 1997) is applied in the broad, soft, medium, hard, and very hard energy bands. The detection threshold we adopted roughly corresponds to 50 spurious sources. We excluded the outermost regions where the selection resulted in a very large number of false positives, resulting in 2306 detected sources.
- The wavelet-based algorithm *Wavdetect* (Freeman et al. 2002) is applied to images in the broad, soft, medium, hard, and very hard energy bands. We set the *sigmathreshold* parameter equal to  $10^{-4}$  and used only two small detection scales, resulting in 2509 detected sources.

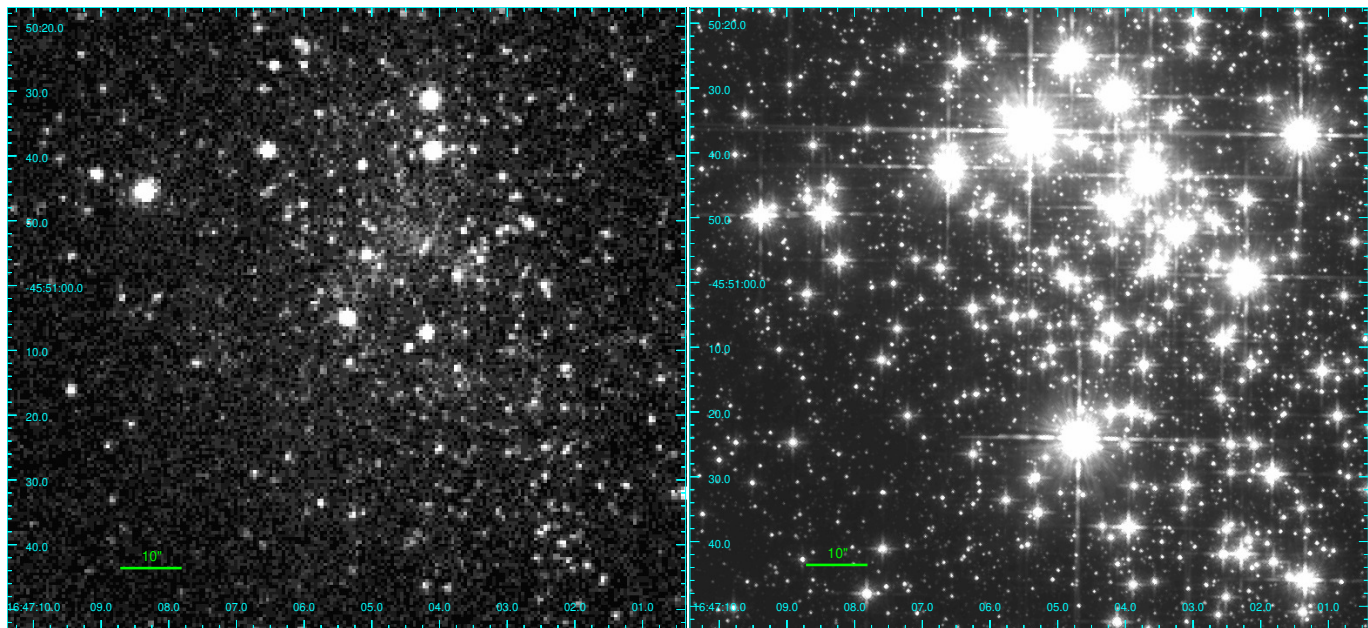
- The maximum likelihood reconstruction method developed by Townsley et al. (2006) is applied in the broad, soft, hard, and very hard energy bands. This algorithm operates over small tiles across the observed field, making it more sensitive to the spatial variation in the PSF and background and thus more capable of detecting faint sources in crowded fields (Broos et al. 2010). The reconstructed image is first calculated using the Lucy-Richardson algorithm (Lucy 1974), and then searched for peaks that identify the positions of point sources. This method resulted in 7585 detected sources.
- A time-resolved deployment of *PWDetect*, described in more details in the following, is performed over segments of 10 ksec of the observations. This method is aimed at detecting faint and variable sources that may only be significant during specific short time segments in which they were detected. This method produced a list of 1147 detected sources.

Figure 5 shows a comparison of the spatial distribution of candidate sources detected using the four methods. In all cases, the cluster appears highly crowded, with the image reconstruction method being the only one capable of detecting a large number of sources in the central region of Westerlund 1, as expected.

#### 4.1. Time-resolved *PWDetect*

We devised a simple time-resolved detection method, tailored to faint transient sources such as magnetically flaring low-mass stars. These may remain undetected in the full dataset because of the high background, but may be detected in a shorter time slice that includes the transient emission, thanks to the enhanced source-counts/background contrast.

We started by considering 10 ks time slices from each observation segment. Since exposure times are not multiple of 10 ks, the exposure time of the last frame was forced to range between 7 ks and 17 ks. Moreover, in order to fully capture transients that would otherwise be split between two frames, we also considered intervals shifted in time by half a frame (5 ks).



**Fig. 4.** Inner region of Westerlund 1 observed with ACIS (left panel) in the broad band and with HST (right panel) using the F160W filter. In the ACIS image, source confusion and a high background intensity dominate the cluster core.

The 44 EWOCS and pre-EWOCS observations were thus split into 194 frames: 106 were 10 ks long, while the duration of the remaining ones are quite uniformly distributed between 5 and 16 ks. For each frame, event lists (and exposure maps) were then extracted in the following five energy bands: 0.5–7.0 keV, 4.0–7.0 keV, 0.5–1.2 keV, 1.2–2.0 keV, and 2.0–7.0 keV, resulting in a total of 970 event files.

We ran *PWDetect* twice on each of these 970 event files, once to estimate the background level and thus evaluate the significance thresholds to obtain the desired number of spurious sources, and once more for the final detection. For the first run we adopted a low significance threshold,  $4.9\sigma$ , so to detect as many sources as possible, but also resulting in several spurious faint sources. The number of background photons was then estimated by subtracting the detected source photons from the total; we then chose the final detection threshold so to yields, on average, 0.1 spurious sources per frame. This was derived from the appropriate significance versus background curve provided by Damiani et al. (1997).

The final *PWDetect* runs produced 944 lists of sources<sup>6</sup> for a total of 14178 sources, most of which are, obviously, repeated detections of the same source in multiple frames and/or bands. We started cleaning up this large sample by removing  $\sim 1600$  extended sources, many of which were unresolved detections of multiple point sources (extent parameter, as given by *PWDetect*, larger than 2). We then screened for the remaining sources for possible cosmic rays afterglow events: for each source we extracted photons from a circle with radius twice the “detection scale” provided by *PWDetect*. In 284 cases the arrival times of all extracted photons were in subsequent 3.14s-long readout frames, and the detection, a likely afterglow artifact was discarded.

All detection lists were cross-identified and merged in a final source list using an iterative procedure: first we cross-identified

and merged the first two catalogs. The resulting catalog was then merged with the third original catalog, and so on for all the 944 catalogs. Identifications were performed searching the close spatial coincidences with identification radii of each original detection taken as the  $1\sigma$  uncertainties as estimated by *PWDetect* (rounded up to 0.5 arcsec if smaller). The coordinates and uncertainties or identification radii of merged sources were computed, at each step, as the uncertainty-weighted means of the coordinates/radii of cross-identified sources<sup>7</sup>. At the end of this process we are left with 1262 cross-matched sources.

Finally, we inspected all the final sources by eye, examining individual detections in the original event file, and the positions in the *Hubble* Space Telescope (HST) *H*-band image (when available, in the field center) and images from the Digitized Sky Survey (DSS) and the Two Micron All-Sky Survey (2MASS). Some cross-identifications were adjusted and a number of “sources,” which were not merged by the automatic process above, were merged as they clearly referred to the same star. The final list counts 1147 sources.

#### 4.2. The merged list of candidate sources

At this stage, we generated a list of candidate sources that includes all the sources detected using the adopted methods. Contamination of this list by false positives is expected to be large, but we relied on the source-validation step, described in the next sections, to prune the catalog from these false and not significant sources.

The lists generated by the four detection methods were cross-matched by eye. In cases where it was difficult to confidently determine the presence of one or more nearby sources, we left

<sup>6</sup> For the observations in standard ACIS-I configuration, detection was performed only on the most on-axis CCD (CCD.ID=7). In 26 cases *PWDetect* crashed or no sources were found. We did not investigate these cases further.

<sup>7</sup> Since most detections are not independent (they may share the same photons because of energy band or overlapping time frames), we computed weighted means only among values belonging to independent groups of positions. Within each group of dependent detections we chose the coordinates and radii of the source with the smallest positional uncertainty.



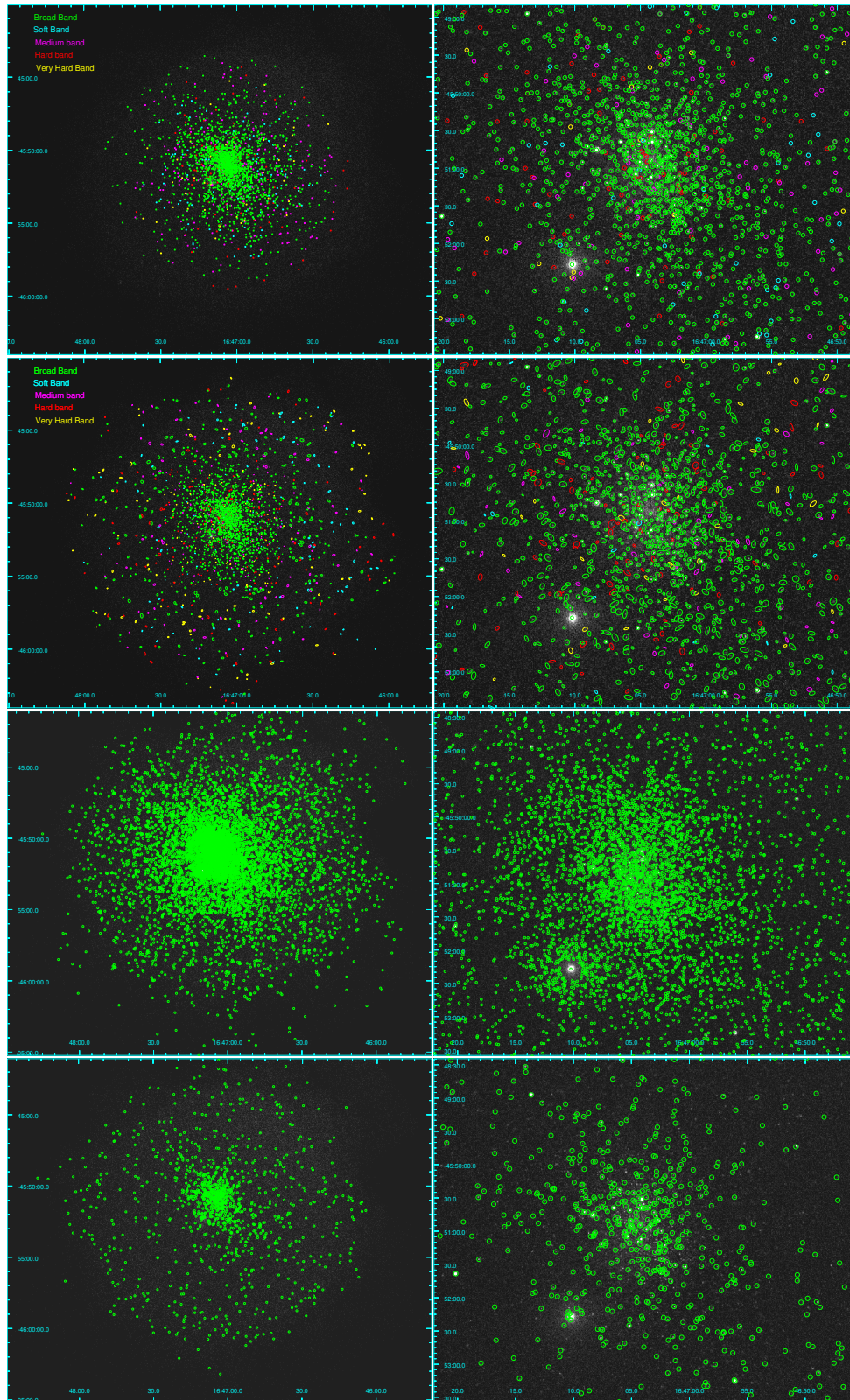


**Fig. 5.** Spatial distribution of candidate sources detected with the four methods (from the top: *Pwdetect*, *Wavdetect*, image reconstruction, and time-resolved *Pwdetect*). The left panels show the whole ACIS field, those on the right the inner region. Different colors in the first and second rows mark sources detected at different energy bands.

those entries unmatched between the catalogs. Additionally, we included in the input list the following sources that were not detected by any of the aforementioned methods:

- 446 faint sources from the catalog presented by Townsley et al. (2018), which are likely not detected in EWOCs observations because of the intrinsic variability of young stars;
- 21 massive stars of Westerlund 1 from the list published by Clark et al. (2020);
- 47 candidate sources added by eye corresponding to the positions of *Gaia* sources in or nearby the cluster center.

The final list of candidate sources, which was used as input for the source validation process in ACIS-Extract (AE), consists of 9420 sources.

## 5. Source extraction, validation, and photometry

Source validation and photometry were performed using the AE software in IDL (Broos et al. 2010)<sup>8</sup>, which has been successfully employed in previous X-ray surveys including the *Chandra* Carina Complex Project (Townsley et al. 2011), the Massive Young Star-forming Complex Study in Infrared and X-Rays (MYStIX) survey (Feigelson et al. 2013), the three Massive Star-forming Regions Omnibus X-ray Catalog (MOCX) data releases (Townsley et al. 2014, 2018, 2019), the *Chandra* Cygnus OB2 Legacy Survey (Wright et al. 2014a), and the Star Formation In Nearby Clouds (SFINC) project (Getman et al. 2017). AE enables the extraction and validation of sources across multiple observations, generating individual source spectra and light curves. It utilizes various data analysis software packages including CIAO, MARX (Davis et al. 2012), HEASoft<sup>9</sup>, and the IDL Astronomy User's Library (Landsman 1993).

Following the guidelines provided by the authors and available on the AE website, we adopted a three-step procedure to compile the X-ray EWOCs catalog:

- Initially, sources were extracted and validated using a parameter defined by AE, which helps distinguish between genuine and false sources. This step was repeated iteratively until no more false sources were identified and removed (Sect. 5.1).
- Subsequently, source positions were updated, followed by another round of source validation process (Sect. 5.2).
- Once the catalog reached a stable state, we performed the photometric procedure, to extract source events comprehensively and calculate the primary spectral and temporal properties for each source across multiple energy bands (Sect. 5.3).

### 5.1. Source validation

The AE procedure assesses the local PSF at the given position of each source and defines extraction regions based on the 1.5 keV local PSF, ensuring they do not overlap with neighboring sources. In the case of close pairs, the extraction region of the fainter source is progressively reduced to prevent overlap until it reaches 40% of its original size. Once this threshold is reached, if the two extraction regions still overlap, AE further reduces the size of the brighter source until the regions no longer overlap. If overlap persists even when both extraction regions are reduced to 40%, AE either discards the specific observation or automatically removes the fainter source.

<sup>8</sup> <https://zenodo.org/records/6084540>

<sup>9</sup> <https://heasarc.gsfc.nasa.gov/lheasoft>

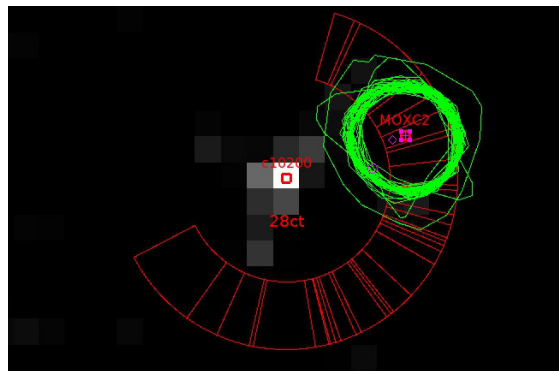


**Fig. 6.** Example of a source (label MOXC2) that was excluded as a potential product of a PSF hook near a brighter source (label c10200). The green contours outline the extraction regions of MOXC2 in all observations, while the red polygons indicate the locations where the PSF hook may appear in each observation, depending on the roll-angle.

The local background is determined within an optimized region surrounding the source. For isolated sources, this region is delimited by an inner radius, which is 1.1 times the radius encompassing 99% of the PSF, and an outer radius large enough to collect at least 100 background events not associated with nearby sources. AE adjusts the size of the background-extraction region to ensure that Poissonian noise contributes no more than 3% to the background uncertainty. However, in crowded regions, defining a region with 100 events may not be feasible. In such cases, AE employs a different calculation that incorporates the contribution from nearby bright sources and a model accounting for the spatial variation of the background.

Source validation relies on a parameter provided by AE called *prob\_no\_source* ( $P_B$ ), which represents the probability that there is no real source at a given position. In our case, where multiple observations of a source are available, AE calculates  $P_B$  based on the extractions with the highest source significance. To differentiate between valid and spurious sources, we applied a threshold of  $P_B=0.01$ , consistent with previous studies. Since the removal of not valid sources could potentially impact the extraction region and background of valid sources, the procedure is iterated until the catalog reaches convergence and no further spurious sources are detected.

After the first iteration, we conducted a visual inspection of sources flagged by AE as potentially resulting from the hook-shaped feature of the PSF<sup>10</sup>. This feature can account for up to 5% of the source flux and its position is influenced by the roll-angle, making it distinguishable from the actual source only in a few cases where the real source is both on-axis and sufficiently bright. Figure 6 illustrates an example of a source (MOXC2) that was flagged by AE as a potential PSF hook and subsequently removed after visual inspection.

AE also identifies sources that are expected to suffer from significant pileup<sup>11</sup> (which is the loss of information due to different incident photons registered as a unique event by the detector). In our case, the only source affected by piled source is the magnetar.

### 5.2. Positions update and visual review

For each source, AE calculates three different position estimates. The first estimate is obtained by taking the mean value of the

<sup>10</sup> [http://cxc.harvard.edu/ciao/caveats/psf\\_artifact.html](http://cxc.harvard.edu/ciao/caveats/psf_artifact.html)

<sup>11</sup> [http://cxc.harvard.edu/ciao/why/pileup\\_intro.html](http://cxc.harvard.edu/ciao/why/pileup_intro.html)



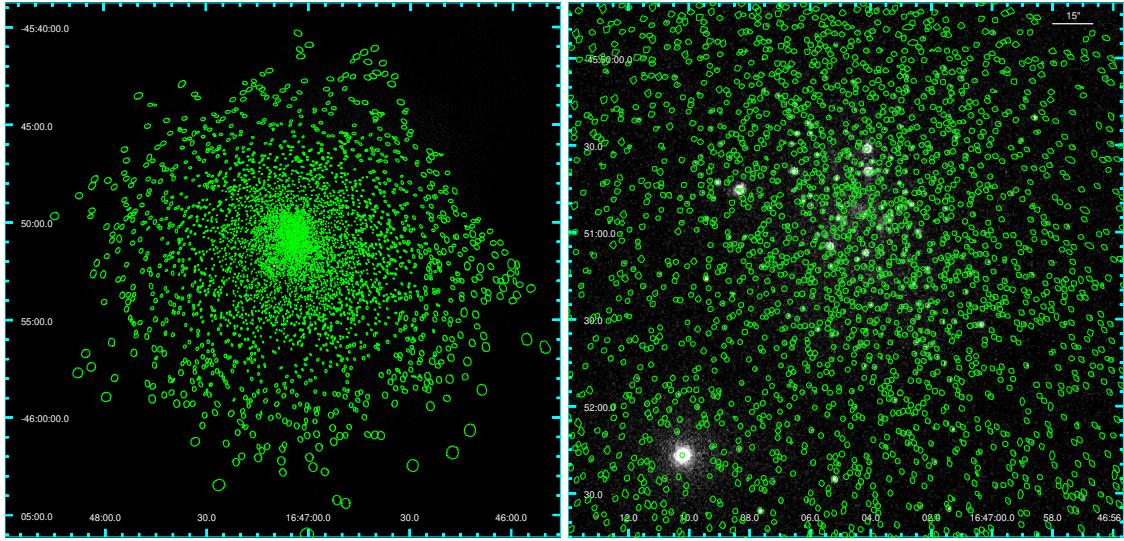


**Fig. 7.** Extraction regions of the validated sources across the entire merged ACIS image (left panel), and extraction regions in the central area of approximately  $3'$  in size (right panel).

positions of the events associated with the source (mean-data position). However, this estimate may be inaccurate for large off-axis angles and in cases where there are significant offsets between the true source position and the extraction region (which can happen when the PSF is asymmetric). To obtain a more accurate estimate in these cases, AE correlates the source PSF with the spatial distribution of extracted events (PSF position). This calculation takes into account the combination of several Obs.IDs by using the PSF calculated in each observation. Both of these estimates can be influenced by nearby sources. In crowded fields, a third estimate is provided by AE using the reconstructed image of the source's neighborhood. It identifies the position of the closest peak in the reconstructed image. According to AE's recommendations, the mean-data position is used for on-axis sources, the PSF position is used for off-axis sources, and the image reconstruction position is used for sources in crowded regions. The repositioning of sources was performed twice, with each step followed by a new sequence of iterations for source validation, as described in the previous section.

Before conducting the visual review of validated sources, the astrometry of both the X-ray sources and the main products file was corrected using the *Gaia*/DR3 astrometric system. After this step, and when catalog stability was achieved again, we conducted a visual review of specific critical sources, including very faint sources that could affect the size of the extraction region of nearby bright sources and suspected afterglows. The decisions made during the visual review were guided also by the presence of high-probability optical and/or infrared counterparts. After the visual review, a new round of source validation was performed.

### 5.3. Spectral extraction

After 21 iterations of the source validation process, the catalog reached stability, with a total of 5963 validated X-ray sources. The final step involved the extraction of X-ray events and the estimation of X-ray properties in 17 energy bands, merging all available observations in a consistent manner. In addition, AE generates light curves and spectra for each source, although these will not be discussed in this paper. AE performs this calculation by

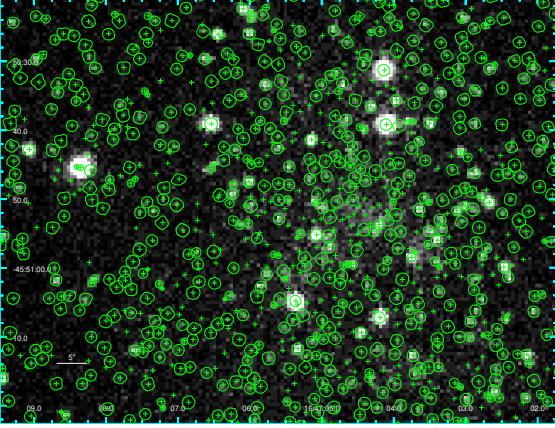
excluding observations where the sources are observed off-axis to improve the overall signal-to-noise ratio. However, in our case, this correction was not necessary due to the design of our survey. The calculated quantities include source counts, net counts, photon flux in  $\text{photon cm}^{-2} \text{s}^{-1}$ , and the quartiles of photons energy.

Figure 7 depicts the spatial distribution of the validated sources in the merged ACIS event files. In the left panel it is evident that there is a high concentration of validated sources toward the center of the cluster, as well as a significant number of sources surrounding the cluster core. This indicates that we have detected stars associated with the extended halo of Westerlund 1. This will be further investigated in upcoming papers of this series, which will focus on source classification and the identification of optical/infrared (OIR) counterparts. The right panel also highlights how this survey has pushed to the limits of *Chandra* in resolving individual stars within such a densely populated stellar cluster with a bright and irregular background. In fact, in the actual core of the cluster, where the background is both intense and variable, a few tens of sources that were initially included as input to AE were subsequently discarded during the validation process (see Fig. 8). The limited number of validated sources in the central region can be attributed to the intense background, and it is likely that many of these discarded sources are indeed genuine X-ray sources. Although we did not attempt to recover these stars, in future papers of this series their candidate OIR counterparts will be analyzed in order to estimate the fraction of real sources that we have excluded.

## 6. The final catalog

It is informative to analyze the number of sources detected using the various methods we employed and assess how many have survived the pruning process. Table 3 presents the total number of input sources for each detection method, as well as the fraction of these sources within  $1''$  and  $3''$  of a source in the final catalog (source positions changed during the pruning process and thus an exact position match was not possible). The image reconstruction method is the only one that experienced significant pruning of the input catalog, as it selects sources that are too faint according to the adopted  $P_B$  threshold. According to





**Fig. 8.** Extraction regions of the validated sources and positions of the input candidate sources (crosses) within the central 1 arcmin region

**Table 3.** EWOCs sources and detection methods.

Detection method	Input N	Within 1''	Within 3''
Image reconstruction	7585	0.29	0.30
<i>PWDetect</i>	2306	0.87	0.92
<i>Wavdetect</i>	2509	0.77	0.82
Time resolved <i>PWDetect</i>	1147	0.77	0.82
Massive stars	21	0.34	0.81
Townsley et al. (2018)	446	0.48	0.66
Added by eye	47	0.38	0.95

Table 3, and considering also that the number of sources in the input *PWDetect* list of candidate sources more distant than 3'' from any source in the Image reconstruction input catalog is low, but not negligible (314, 688 for *Wavdetect*), it is evident that in complex fields like these, deploying different detection methods is crucial for optimizing the number of detected sources.

Given the design of the EWOCs survey and the compact nature of Westerlund 1, it is not surprising that the majority of sources are observed at low off-axis angles, as depicted in Fig. 9. Specifically, 63.7% of the sources (3485/5464) are located within 1 arcmin from the field center, and 87.7% are within 3 arcmin. Consequently, source positions are generally well-determined, with a median position error of 0.17'' and a 75% quantile position error of 0.27''. Position errors are estimated from the single-axis standard deviations of the PSF inside the extraction region and the number of counts extracted. This precision is crucial for the search of OIR counterparts and for dynamics studies.

As depicted in Fig. 10, the catalog is predominantly composed of faint sources. In the broad band, the median value of the net counts is 12.9 counts. There are 607 sources (10.2%) with fewer than 5 net counts and only 69 sources (1.2%) with fewer than 3 counts. It is well known that the sensitivity of ACIS-I decreases with the off-axis angle. This must be taken in consideration when comparing the spatial distribution of X-ray sources detected with ACIS-I to those detected with other instruments. Figure 11 illustrates the spatial distributions of EWOCs X-ray sources with fewer than 12.9 net counts and those with more net counts. The former sample exhibits a higher concentration in the center of the field, with only 37 sources having an off-axis angle larger than 7'. This region is considerably large compared to the

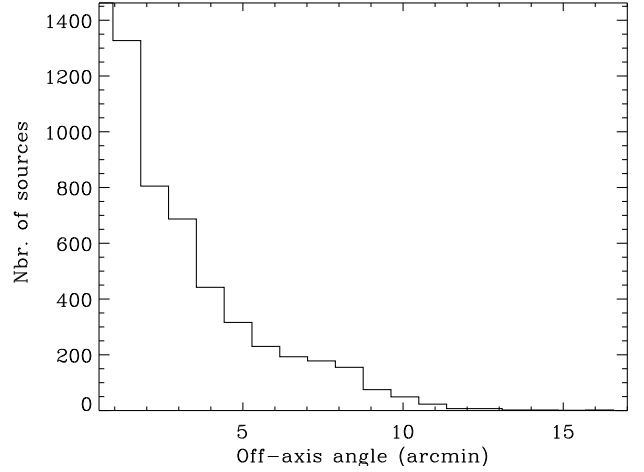


**Fig. 9.** Distribution of the off-axis angles of the EWOCs X-ray sources.

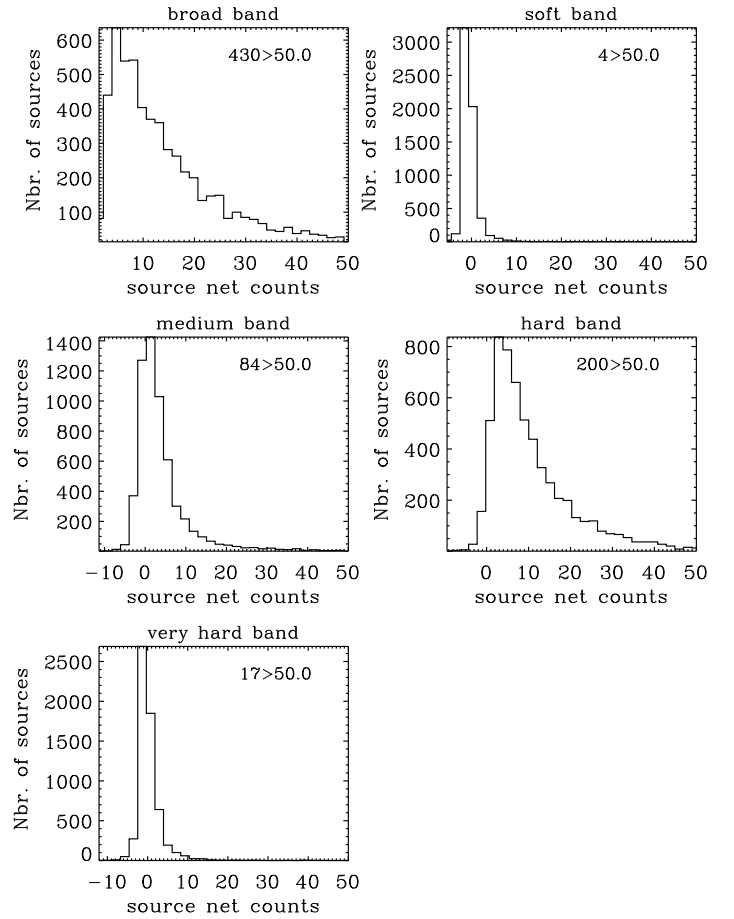


**Fig. 10.** Distributions of source net counts in the broad, soft, medium, hard, and very hard energy bands. The number of sources with more than 50 counts is indicated in the top-right corner of each panel.

size of Westerlund 1, so studies based on the spatial distribution of cluster members would not be significantly affected by the decline in sensitivity with the off-axis angle.

Given the design of the EWOCs observations and the intricate procedure we employed for source detection and validation, it is not currently feasible to provide a reliable estimate of catalog completeness without making strong and unverified assumptions about cluster properties, its morphology, and both mass

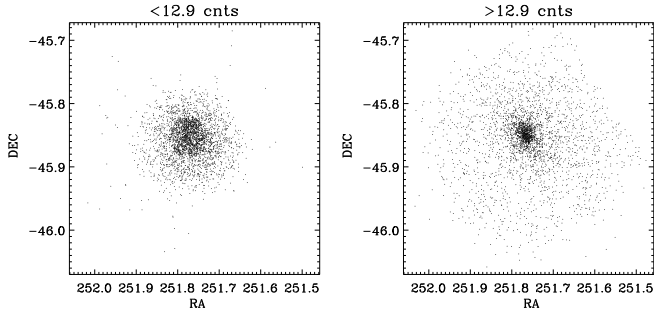


**Fig. 11.** Spatial distribution of EWOCs X-ray sources, sorted into two bins based on their net counts in the broad band.

and  $L_X$  distributions. Instead, we prefer to discuss the achieved completeness in future papers of this series, once the identification of OIR counterparts and the determination of true cluster members have been accomplished. In Appendix C, however, we present a simplified analysis of completeness based on different assumptions regarding cluster morphology, along with simulations conducted using the MARX simulator.

The distribution of the median photon energy for the EWOCs X-ray sources is shown in Fig. 12. The median value of the distribution is 2.8 keV. In the case of young stellar populations in clusters with low extinction, the median photon energy serves as a reliable indicator of membership since the coronal plasma temperature in young stars is typically higher than in older stars. However, since interstellar absorption is significant in the direction of Westerlund 1, it becomes challenging to differentiate between the absorbed background population and the young stars within the cluster. However, the secondary peak observed at energies below 2 keV in the  $E_{\text{med}}$  distribution could potentially be attributed to a foreground population. Nevertheless, the spatial distribution of these soft sources does not differ significantly from that of the more energetic sources. Additionally, Fig. 12 includes a comparison between the photon median energy distribution of the EWOCs X-ray sources and the X-ray catalog published by Townsley et al. (2018) based on pre-EWOCs observations, which clearly exhibits a peak below 2 keV. The evident differences in the two distributions can be due to a combination of factors: the presence of a large population of stars associated with Westerlund 1 in the EWOCs catalog (which is a factor of  $\sim 5$  deeper in X-ray photon flux compared to the catalog published by Townsley et al. 2018, considering the faintest sources in the two catalogs), as well as the decline in sensitivity in the soft band of the ACIS detector with the years, and the better sensitivity toward soft events of the ACIS-S detector compared with ACIS-I.

The catalog also includes a measure of source flux provided by AE: the photon flux ( $F_{\text{photons}}$ ), which is calculated as the ratio of the source net counts to the product of the mean effective area and nominal exposure time (thus expressed in units of photons  $\text{cm}^{-2} \text{s}^{-1}$ ). A model-independent estimate of the apparent source energy flux can be calculated as  $1.602 \times 10^{-9} \times E_{\text{med}} \times F_{\text{photons}}$ . The coefficient is derived from the conversion between keV and erg, as determined by Getman et al. (2010).

In Appendix A, we show ten rows of the X-ray EWOCs catalog, which is available in full at the CDS. We have also made the output table produced by AE available on the EWOCs website in its original IDL format<sup>12</sup>.

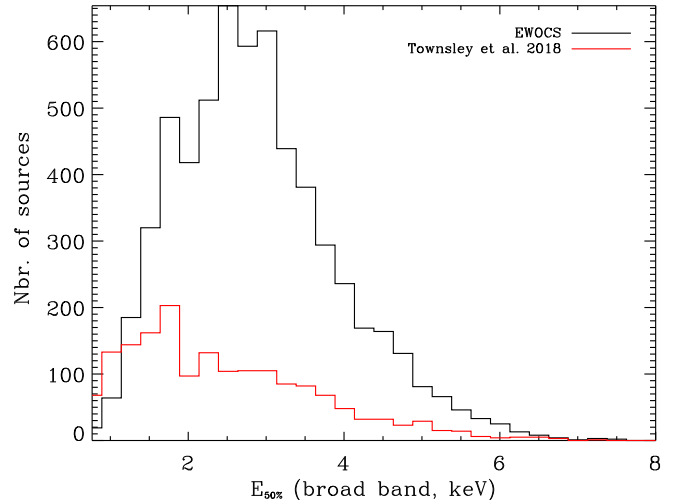


**Fig. 12.** Distribution of the median photon energy in the broad band for the validated EWOCs X-ray sources (black) and the catalog published by Townsley et al. (2018), in red.

## 7. Specific sources

Not surprisingly, CXOU J16 is the brightest source in the EWOCs X-ray catalog, with a total of  $71\,601 \pm 268$  net counts collected and a photon flux of  $3.45 \times 10^{-4}$  photons  $\text{cm}^{-2} \text{s}^{-1}$ . The source, which is strongly piled-up, is quite isolated and produces a surrounding bright background, with the closest source being at about 8 arcsec. The pulsar will be analyzed in detail in future papers of this project.

As explained in Sect. 2, Westerlund 1 hosts a unique ensemble of massive stars caught in different evolutionary stages. Understanding the mechanisms responsible for the emission of X-rays and studying both binarity and the circumstellar environment in these stars is of primary importance for EWOCs. We visually inspected the X-ray counterparts of massive stars published by Clark et al. (2020) and found 126 coincidences out of the 166 listed massive stars. The results are listed in Table B.1. In the vast majority of cases, there was a clear one-to-one correspondence between the sources in the two catalogs. There are a few uncertain cases, which can be easily identified by repeated massive star IDs, EWOCs objects, or large separations.

The brightest X-ray massive star in the EWOCs catalog is the SgB[e] star W9 (Clark et al. 2014), with nearly 8000 net counts collected in the broad band. The intense X-ray brightness ( $L_X \sim 3.6 \times 10^{33}$  erg  $\text{s}^{-1}$ ) and the hardness of the spectrum, as previously reported by Clark et al. (2008), are consistent with the evidence of intense mass loss rate, estimated to be around  $10^{-5} M_{\odot} \text{yr}^{-1}$  (Andrews et al. 2019), and strong indications of binarity (Ritchie et al. 2022). W9 is the brightest source in the cluster also at radio wavelengths (Andrews et al. 2019), millimeter band (Fenech et al. 2018), and it shows very bright mid-IR emission (Clark et al. 1998).

In terms of X-ray luminosity, W9 is followed by the post-binary blue straggler W30 (O4-5Ia<sup>+</sup>; Clark et al. 2019, 2008), for which a putative orbital period of approximately 6.2 days has been identified from a radial velocity series analyzed by Ritchie et al. (2022). We have detected nearly 6000 net counts in the broad band for W30. After W9 and W30, the list of sources with net counts ranging between 190 and 5400 photons includes most of the known WR stars and OB supergiant binary systems.

The deep EWOCs observations provide, for the first time, candidate X-ray detections for some normal giant and subgiant

<sup>12</sup> <https://westerlund1survey.wordpress.com/>

stars, such as W50b and W1051. The lack of detection in the pre-EWOCS observations has been explained as a natural consequence of the lower intrinsic bolometric luminosity of these stars compared to more evolved massive stars in the cluster (Clark et al. 2019). The detection in the EWOCS observations supports this hypothesis. Faint X-ray counterparts have also been found for the two YHGs W4 and W8 (with 22 and 73 net counts, respectively), whose nature has been recently discussed by Beasor et al. (2023), who classified them as yellow supergiants. Additionally, a faint counterpart has been detected for the BHG W1049 (with  $14.16_{8.4}^{20.4}$  net counts). For the first time, faint counterparts have been found for the four O9.5II SB1 stars W1022, W1050, W1056, and W1060, as well as for the B1.5II star W1048. We also confirm the relatively faint ( $75.75_{65.8}^{85.7}$  net counts) and soft (median photon energy of 1.9 keV) X-ray emission from the SB2 star (B0.5I+OB) W10, as previously reported by Clark et al. (2008). Ritchie et al. (2022) attributed the X-ray properties of this star to the possibility that the pre-EWOCS observations were made at a phase where the wind collision zone was weak or obscured. However, given the length of the EWOCS observations, it is more likely that these properties are intrinsic to the star.

It is quite interesting that out of the 124 sources in our catalog with more than 100 net counts, 94 do not readily match any known massive stars in the cluster. This subset will be studied in detail in future works of this series to determine their nature. It is intriguing that this sample does not seem to follow the distribution of photon energy shown in Fig. 12. In fact, its photon median energy distribution exhibits three distinct peaks: one below 2 keV (which may be dominated by foreground stars), one between 2.5 keV and 3 keV (compatible with cluster stars), and one between 3.8 keV and 4.3 keV (which could be influenced by background sources or flaring low-mass cluster members).

We also provide a list of positions for the unvalidated candidate X-ray sources on the EWOCS website<sup>13</sup>. This list will be cross-matched with existing optical and infrared catalogs of Westerlund 1 to determine the fraction of rejected sources that could potentially be true counterparts of cluster members. Likewise, identifying optical and infrared counterparts will enable us to assess the level of contamination and the fraction of expected spurious sources in the EWOCS X-ray source catalog, as well as determine the completeness limit achieved by our survey.

## 8. Conclusions

In this paper, we present the EWOCS project and a new list of X-ray sources in the young supermassive star cluster Westerlund 1 and its surrounding area. The EWOCS project aims to investigate the impact of the starburst environment on the formation process of stars and planets, the dispersal of protoplanetary disks, and the evolutionary pathway of massive stars.

Here we present the 1 Msec *Chandra*/ACIS-I EWOCS observations of Westerlund 1, the workflow for data reduction, the procedure for source detection and validation, and the spectral extraction of the validated sources. Initially, we generated a preliminary list of 9420 candidate X-ray sources using the image reconstruction method, *PWDetect*, *WAVDETECT*, and a specific deployment of *PWDetect* focused on identifying flaring stars that exhibited a significant signal above the background for a brief duration. Additionally, a few sources were manually added or obtained from existing catalogs of Westerlund 1 sources. From

these input sources, we compiled the EWOCS catalog of X-ray sources in Westerlund 1 of 5963 sources successfully validated using the IDL-based software AE.

The median value of net counts in the EWOCS X-ray catalog is approximately 13 counts, with about 10% of sources having fewer than 5 net counts detected in the broad energy band. The distribution of the median photon energy of the sources peaks at approximately 2.8 keV, with a contribution from unrelated (foreground and background) sources that is challenging to distinguish from the candidate cluster members. The brightest source in the catalog is the magnetar CXO J164710.2-455216, with over 70 000 net counts detected in the broad band. It is followed by several massive stars in Westerlund 1, including the SgB[e] star W9, the post-binary blue straggler W30, and some WR stars and supergiants in binary systems. Out of the 166 known very massive stars in Westerlund 1, we have identified a reliable X-ray counterpart for 126 of them. Additionally, we have made the first detection of an extended and rich halo surrounding the core of Westerlund 1, which will be crucial in assessing the cluster's true mass content, formation, and evolution.

*Acknowledgements.* We acknowledge the referee for his/her careful reading of our paper and suggestions. M.G.G. is also indebted to Leisa K. Townsley and Patrick S. Broos for their valuable suggestions and advice on data reduction and ACIS extraction. M.G.G., C.A., R.B., E.F., G.L.I., L.P., and S.S. acknowledge the INAF grant 1.05.12.05.03. K.M. acknowledges support from the Fundação para a Ciência e a Tecnologia (FCT) through the CEEC-individual contract 2022.03809.CEECIND and research grants UIDB/04434/2020 and UIDP/04434/2020. Support for this work was also provided by the National Aeronautics and Space Administration through *Chandra* Proposal 21200267 issued by the *Chandra* X-ray Center, which is operated by the Smithsonian Astrophysical Observatory for and on behalf of the National Aeronautics Space Administration under contract NAS8-03060. I.N. is partially supported by the Spanish Government Ministerio de Ciencia e Innovación (MCIN) and Agencia Estatal de Investigación (MCIN/AEI/10.13039/501100011033/FEDER, UE) under grant PID2021-122397NB-C22, and also by MCIN with funding from the European Union NextGenerationEU and Generalitat Valenciana in the call Programa de Planes Complementarios de I+D+i (PRTR 2022), project HIAMAS, reference ASFAE/2022/017. M. G. G. and R. B. acknowledge partial support from the Grant INAF 2022 YODA; R. B. also acknowledges partial support from the project PRIN-INAF 2019 “Spectroscopically Tracing the Disk Dispersal Evolution”. The scientific results reported in this article are based on observations made by the *Chandra* X-ray Observatory. M.M. acknowledges financial support from the European Research Council for the ERC Consolidator grant DEMOBLACK, under contract no. 770017, and from the German Excellence Strategy via the Heidelberg Cluster of Excellence (EXC 2181 – 390900948) STRUCTURES.

## References

- Adamo, A., Zeidler, P., Kruijssen, J. M. D., et al. 2020, *Space Sci. Rev.*, **216**, 69  
 Aghakhanloo, M., Murphy, J. W., Smith, N., et al. 2020, *MNRAS*, **492**, 2497  
 An, H., Kaspi, V. M., Archibald, R., & Cumming, A. 2013, *ApJ*, **763**, 82  
 Andersen, M., Gennaro, M., Brandner, W., et al. 2017, *A&A*, **602**, A22  
 Andrews, H., Fenech, D., Prinja, R. K., Clark, J. S., & Hindson, L. 2019, *A&A*, **632**, A38  
 Barrado, D., Stelzer, B., Morales-Calderón, M., et al. 2011, *A&A*, **526**, A21  
 Beasor, E. R., Davies, B., Smith, N., Gehrz, R. D., & Figer, D. F. 2021, *ApJ*, **912**, 16  
 Beasor, E. R., Smith, N., & Andrews, J. E. 2023, *ApJ*, **952**, 113  
 Benjamin, R. A., Churchwell, E., Babler, B. L., et al. 2003, *PASP*, **115**, 953  
 Berghoefter, T. W., Schmitt, J. H. M. M., & Cassinelli, J. P. 1996, *A&AS*, **118**, 481  
 Borgehe, A., Rea, N., Turolla, R., et al. 2019, *MNRAS*, **484**, 2931  
 Brandner, W., Clark, J. S., Stolte, A., et al. 2008, *A&A*, **478**, 137  
 Broos, P. S., Townsley, L. K., Feigelson, E. D., et al. 2010, *ApJ*, **714**, 1582  
 Clark, J. S., & Negueruela, I. 2002, *A&A*, **396**, L25  
 Clark, J. S., & Negueruela, I. 2004, *A&A*, **413**, L15  
 Clark, J. S., Fender, R. P., Waters, L. B. F. M., et al. 1998, *MNRAS*, **299**, L43  
 Clark, J. S., Negueruela, I., Crowther, P. A., & Goodwin, S. P. 2005, *A&A*, **434**, 949  
 Clark, J. S., Munro, M. P., Negueruela, I., et al. 2008, *A&A*, **477**, 147  
 Clark, J. S., Negueruela, I., Davies, B., et al. 2009, *A&A*, **498**, 109

<sup>13</sup> <https://westerlund1survey.wordpress.com/>



- Clark, J. S., Negueruela, I., & González-Fernández, C. 2014, *A&A*, **561**, A15
- Clark, J. S., Najarro, F., Negueruela, I., et al. 2019, *A&A*, **623**, A83
- Clark, J. S., Ritchie, B. W., & Negueruela, I. 2020, *A&A*, **635**, A187
- Crowther, P. A., Hadfield, L. J., Clark, J. S., Negueruela, I., & Vacca, W. D. 2006, *MNRAS*, **372**, 1407
- D'Ai, A., Evans, P. A., Krimm, H. A., et al. 2017, *GRB Coordinates Network*, **21095**, 1
- Damiani, F., Maggio, A., Micela, G., & Sciortino, S. 1997, *ApJ*, **483**, 350
- Damineli, A., Almeida, L. A., Blum, R. D., et al. 2016, *MNRAS*, **463**, 2653
- Davies, B., & Beasor, E. R. 2019, *MNRAS*, **486**, L10
- Davies, B., Figer, D. F., Kudritzki, R.-P., et al. 2007, *ApJ*, **671**, 781
- Davies, B., de La Fuente, D., Najarro, F., et al. 2012, *MNRAS*, **419**, 1860
- Davis, J. E., Bautz, M. W., Dewey, D., et al. 2012, *SPIE Conf. Ser.*, **8443**, 84431A
- de Grijs, R., O'Connell, R. W., & Gallagher, John S., I. 2001, *AJ*, **121**, 768
- de Grijs, R., Anders, P., Bastian, N., et al. 2003a, *MNRAS*, **343**, 1285
- de Grijs, R., Fritze-v. Alvensleben, U., Anders, P., et al. 2003b, *MNRAS*, **342**, 259
- de la Fuente, D., Najarro, F., Borissova, J., et al. 2016, *A&A*, **589**, A69
- Dougherty, S. M., Clark, J. S., Negueruela, I., Johnson, T., & Chapman, J. M. 2010, *A&A*, **511**, A58
- Dunlop, J. S. 2011, *Science*, **333**, 178
- Eufrazio, R. T., Lehmer, B. D., Zezas, A., et al. 2017, *ApJ*, **851**, 10
- Feigelson, E. D., Townsley, L. K., Broos, P. S., et al. 2013, *ApJS*, **209**, 26
- Fenech, D. M., Clark, J. S., Prinja, R. K., et al. 2018, *A&A*, **617**, A137
- Figer, D. F. 2008, in *Massive Stars as Cosmic Engines*, 250, eds. F. Bresolin, P. A. Crowther, & J. Puls, 247
- Figer, D. F., McLean, I. S., & Morris, M. 1999, *ApJ*, **514**, 202
- Figer, D. F., Najarro, F., Gilmore, D., et al. 2002, *ApJ*, **581**, 258
- Figer, D. F., MacKenty, J. W., Robberto, M., et al. 2006, *ApJ*, **643**, 1166
- Freeman, P. E., Kashyap, V., Rosner, R., & Lamb, D. Q. 2002, *ApJS*, **138**, 185
- Fruscione, A., McDowell, J. C., Allen, G. E., et al. 2006, *Proc. SPIE*, **6270**, 62701V
- Gaia Collaboration (Brown, A. G. A., et al.) 2016, *A&A*, **595**, A2
- Gaia Collaboration (Vallenari, A., et al.) 2023, *A&A*, **674**, A1
- Garmire, G. P., Bautz, M. W., Ford, P. G., Nousek, J. A., & Ricker, Jr., G. R. 2003, *SPIE Conf. Ser.*, **4851**, 28
- Gennaro, M., Brandner, W., Stolte, A., & Henning, T. 2011, *MNRAS*, **412**, 2469
- Getman, K. V., Flaccomio, E., Broos, P. S., et al. 2005, *ApJS*, **160**, 319
- Getman, K. V., Feigelson, E. D., Broos, P. S., Townsley, L. K., & Garmire, G. P. 2010, *ApJ*, **708**, 1760
- Getman, K. V., Broos, P. S., Kuhn, M. A., et al. 2017, *ApJS*, **229**, 28
- Groh, J. H., Damineli, A., Teodoro, M., & Barbosa, C. L. 2006, *A&A*, **457**, 591
- Hachisuka, K., Brunthaler, A., Menten, K. M., et al. 2006, *ApJ*, **645**, 337
- Hopkins, A. M., & Beacom, J. F. 2006, *ApJ*, **651**, 142
- Israel, G. L., Campana, S., Dall'Osso, S., et al. 2007, *ApJ*, **664**, 448
- Israel, G. L., Esposito, P., & Rea, N. 2011, *ATel*, **3653**, 1
- Kavanagh, P. J., Norci, L., & Meurs, E. J. A. 2011, *New A*, **16**, 461
- Kothes, R., & Dougherty, S. M. 2007, *A&A*, **468**, 993
- Koumpia, E., & Bonanos, A. Z. 2012, *A&A*, **547**, A30
- Krimm, H., Barthelmy, S., Campana, S., et al. 2006, *GRB Coordinates Network*, **5581**, 1
- Kroupa, P. 2001, *MNRAS*, **322**, 231
- Kudryavtseva, N., Brandner, W., Gennaro, M., et al. 2012, *ApJ*, **750**, L44
- Landsman, W. B. 1993, in *ASP Conf. Ser.*, 52, *Astronomical Data Analysis Software and Systems II*, eds. R. J. Hanisch, R. J. V. Brissenden, & J. Barnes, 246
- Larson, R. B., & Tinsley, B. M. 1978, *ApJ*, **219**, 46
- Licquia, T. C., & Newman, J. A. 2015, *ApJ*, **806**, 96
- Lim, B., Chun, M.-Y., Sung, H., et al. 2013, *AJ*, **145**, 46
- Lucy, L. B. 1974, *AJ*, **79**, 745
- Mackey, J., Castro, N., Fossati, L., & Langer, N. 2015, *A&A*, **582**, A24
- Madau, P., & Dickinson, M. 2014, *ARA&A*, **52**, 415
- Mahy, L., Lanthermann, C., Hutsemékers, D., et al. 2022, *A&A*, **657**, A4
- Meingast, S., Alves, J., & Rottensteiner, A. 2021, *A&A*, **645**, A84
- Melena, N. W., Massey, P., Morrell, N. I., & Zangari, A. M. 2008, *AJ*, **135**, 878
- Montmerle, T. 1996, in *ASP Conf. Ser.*, 109, *Cool Stars, Stellar Systems, and the Sun*, eds. R. Pallavicini, & A. K. Dupree, 405
- Muno, M. P., Clark, J. S., Crowther, P. A., et al. 2006, *ApJ*, **636**, L41
- Navarete, F., Damineli, A., Ramirez, A. E., Rocha, D. F., & Almeida, L. A. 2022, *MNRAS*, **516**, 1289
- Negueruela, I., & Clark, J. S. 2005, *A&A*, **436**, 541
- Negueruela, I., Clark, J. S., & Ritchie, B. W. 2010, *A&A*, **516**, A78
- Negueruela, I., Alfaro, E. J., Dorda, R., et al. 2022, *A&A*, **664**, A146
- Perna, R., & Pons, J. A. 2011, *ApJ*, **727**, L51
- Piatti, A. E., Bica, E., & Claria, J. J. 1998, *A&AS*, **127**, 423
- Pineda, J. L., Fischer, C., Kapala, M., et al. 2018, *ApJ*, **869**, L30
- Portegies Zwart, S. F., Baumgardt, H., Hut, P., Makino, J., & McMillan, S. L. W. 2004, *Nature*, **428**, 724
- Preibisch, T., & Feigelson, E. D. 2005, *ApJS*, **160**, 390
- Preibisch, T., Kim, Y.-C., Favata, F., et al. 2005, *ApJS*, **160**, 401
- Prisinzano, L., Damiani, F., Sciortino, S., et al. 2022, *A&A*, **664**, A175
- Rieke, G. H., & Rujopakarn, W. 2011, in *ASP Conf. Ser.*, 446, *Galaxy Evolution: Infrared to Millimeter Wavelength Perspective*, eds. W. Wang, J. Lu, Z. Luo, et al. 3
- Ritchie, B. W., Clark, J. S., Negueruela, I., & Crowther, P. A. 2009, *A&A*, **507**, 1585
- Ritchie, B. W., Clark, J. S., Negueruela, I., & Langer, N. 2010, *A&A*, **520**, A48
- Ritchie, B. W., Clark, J. S., Negueruela, I., & Najarro, F. 2022, *A&A*, **660**, A89
- Robitaille, T. P., & Whitney, B. A. 2010, *ApJ*, **710**, L11
- Rygl, K. L. J., Brunthaler, A., Sanna, A., et al. 2012, *A&A*, **539**, A79
- Salpeter, E. E. 1955, *ApJ*, **121**, 161
- Seward, F. D., Forman, W. R., Giacconi, R., et al. 1979, *ApJ*, **234**, L55
- Skinner, S. L., Simmons, A. E., Zhekov, S. A., et al. 2006, *ApJ*, **639**, L35
- Smith, B. J., & Struck, C. 2010, *AJ*, **140**, 1975
- Smith, N., Vink, J. S., & de Koter, A. 2004, *ApJ*, **615**, 475
- Townsley, L. K., Feigelson, E. D., Montmerle, T., et al. 2003, *ApJ*, **593**, 874
- Townsley, L. K., Broos, P. S., Feigelson, E. D., et al. 2006, *AJ*, **131**, 2140
- Townsley, L. K., Broos, P. S., Corcoran, M. F., et al. 2011, *ApJS*, **194**, 1
- Townsley, L. K., Broos, P. S., Garmire, G. P., et al. 2014, *ApJS*, **213**, 1
- Townsley, L. K., Broos, P. S., Garmire, G. P., et al. 2018, *ApJS*, **235**, 43
- Townsley, L. K., Broos, P. S., Garmire, G. P., & Povich, M. S. 2019, *ApJS*, **244**, 28
- van Leeuwen, F., de Bruijne, J., Babusiaux, C., et al. 2021, *Gaia EDR3 documentation*, European Space Agency; Gaia Data Processing and Analysis Consortium. Online at <https://gea.esac.esa.int/archive/documentation/GEDR3/index.html>
- Vargas Álvarez, C. A., Kobulnicky, H. A., Bradley, D. R., et al. 2013, *AJ*, **145**, 125
- Weisskopf, M. C., Brinkman, B., Canizares, C., et al. 2002, *PASP*, **114**, 1
- Westerlund, B. 1961, *PASP*, **73**, 51
- Westerlund, B. E. 1968, *ApJ*, **154**, L67
- Wright, N. J., Drake, J. J., Guarcello, M. G., et al. 2014a, ArXiv e-prints [arXiv:1408.6579]
- Wright, N. J., Wesson, R., Drew, J. E., et al. 2014b, *MNRAS*, **437**, L1

- 
- <sup>1</sup> Istituto Nazionale di Astrofisica (INAF) — Osservatorio Astronomico di Palermo, Piazza del Parlamento 1, 90134 Palermo, Italy  
e-mail: mario.guarcello@inaf.it
  - <sup>2</sup> Universidad de Río Negro, Sede Atlántica – CONICET, Viedma CP8500, Río Negro, Argentina
  - <sup>3</sup> Instituto de Astrofísica e Ciências do Espaço, Faculdade de Ciências, Universidade de Lisboa, Ed. C8, Campo Grande, 1749-016 Lisbon, Portugal
  - <sup>4</sup> European Southern Observatory, Karl-Schwarzschild-Strasse 2, 85748 Garching bei München, Germany
  - <sup>5</sup> Department of Physics and Chemistry, University of Palermo, Palermo, Italy
  - <sup>6</sup> Donostia International Physics Center (DIPC), Paseo Manuel de Lardizabal, 4, 20018 Donostia-San Sebastián, Guipuzkoa, Spain
  - <sup>7</sup> IKERBASQUE, Basque Foundation for Science, 48013 Bilbao, Spain
  - <sup>8</sup> Astrophysics Research Institute, Liverpool John Moores University, IC2 Liverpool Science Park, 146 Brownlow Hill, Liverpool L3 5RF, UK
  - <sup>9</sup> Space Sciences, Technologies and Astrophysics Research (STAR) Institute, University of Liège, Quartier Agora, 19c, Allée du 6 Août, B5c, 4000 Sart Tilman, Belgium
  - <sup>10</sup> Instituto de Astrofísica de Canarias, 38205 La Laguna, Tenerife, Spain
  - <sup>11</sup> Departamento de Astrofísica, Universidad de La Laguna, 38206 La Laguna, Tenerife, Spain
  - <sup>12</sup> Departamento de Astrofísica, Centro de Astrobiología, (CSIC-INTA), Ctra. Torrejón a Ajalvir, km 4, Torrejón de Ardoz, 28850 Madrid, Spain

- <sup>13</sup> School of Physical Sciences, The Open University, Walton Hall, Milton Keynes MK7 6AA, UK
- <sup>14</sup> Institute of Astronomy, University of Cambridge, Madingley Road, Cambridge CB3 0HA, UK
- <sup>15</sup> Institute of Space Sciences (ICE, CSIC), Campus UAB, Carrer de Can Magrans s/n, 08193 Barcelona, Spain
- <sup>16</sup> Institut d'Estudis Espacials de Catalunya (IEEC), Carrer Gran Capitá 2–4, 08034 Barcelona, Spain
- <sup>17</sup> Center for Astrophysics | Harvard & Smithsonian, 60 Garden Street, Cambridge, MA 02138, USA
- <sup>18</sup> Department of Astronomy, University of Florida, PO Box 112055, Gainesville, FL 32611-2055, USA
- <sup>19</sup> Istituto Nazionale di Astrofisica (INAF) – Osservatorio Astronomico di Roma, Via Frascati 33, 00078 Monte Porzio Catone, Italy
- <sup>20</sup> Universität Heidelberg, Zentrum für Astronomie, Institut für Theoretische Astrophysik, Albert-Ueberle-Str. 2, 69120 Heidelberg, Germany
- <sup>21</sup> Physics and Astronomy Department Galileo Galilei, University of Padova, Vicolo dell'Osservatorio 3, 35122 Padova, Italy
- <sup>22</sup> Univ. Grenoble-Alpes, CNRS, IPAG, 38000 Grenoble, France
- <sup>23</sup> Departamento de Física Aplicada, Facultad de Ciencias, Universidad de Alicante, Carretera de San Vicente s/n, 03690, San Vicente del Raspeig, Spain
- <sup>24</sup> Dipartimento di Fisica e Astronomia, Università di Bologna, Via Gobetti 93/2, Bologna 40129, Italy
- <sup>25</sup> Istituto Nazionale di Astrofisica (INAF) – Osservatorio di Astrofisica e Scienza dello Spazio di Bologna, Via Gobetti 93/3, Bologna 40129, Italy
- <sup>26</sup> Space Telescope Science Institute, 3700 San Martin Dr, Baltimore, MD 21218, USA
- <sup>27</sup> School of Physics & Astronomy, University of St Andrews, North Haugh, St Andrews KY16 9SS, UK
- <sup>28</sup> Istituto Nazionale di Astrofisica (INAF) — Osservatorio Astrofisico di Catania, Via Santa Sofia 78, 95123 Catania, Italy
- <sup>29</sup> Université Côte d'Azur, Observatoire de la Côte d'Azur, CNRS, Laboratoire Lagrange, 06300 Nice, France; Université Grenoble Alpes, CNRS, IPAG, 38000 Grenoble, France
- <sup>30</sup> Astrophysics Group, Keele University, Keele, Staffordshire ST5 5BG, UK
- <sup>31</sup> University of Split, Faculty of Science, Department of Physics, Rudera Boškovića 33, 21000 Split, Croatia
- <sup>32</sup> Johns Hopkins University, 3400 N. Charles Street, Baltimore, MD 21218, USA
- <sup>33</sup> Department of Astronomy, University of Massachusetts, 710 North Pleasant Street, Amherst, MA 01003, USA
- <sup>34</sup> AURA for the European Space Agency (ESA), ESA Office, Space Telescope Science Institute, 3700 San Martin Drive, Baltimore, MD 21218, USA
- <sup>35</sup> The William H. Miller III Department of Physics & Astronomy, Bloomberg Center for Physics and Astronomy, Johns Hopkins University, 3400 N. Charles Street, Baltimore, MD 21218, USA
- <sup>36</sup> Department of Astronomy, University of Texas at Austin, Austin, TX 78712, USA
- <sup>37</sup> Centre for Astrophysics and Supercomputing, Swinburne University of Technology, PO Box 218, Hawthorn VIC 3122, Australia
- <sup>38</sup> Department of Physics & Astronomy, University College London, Gower Street, London WC1E 6BT, UK
- <sup>39</sup> Astronomisches Rechen-Institut, Zentrum für Astronomie der Universität Heidelberg, Mönchhofstr. 12–14, 69120 Heidelberg, Germany

## **Appendix A: Extract of the EWOCs X-ray Westerlund 1 sources catalog**

Ten rows of the EWOCs catalog of the X-ray sources in Westerlund 1 are shown here. The full catalog is available at the CDS.



**Table A.1.** Ten rows extracted from the EWOCs catalog of the X-ray sources in Westerlund 1

EWOCs-X ID	Catalog name <sup>(a)</sup>	Astrometry				Photometry					
		$\alpha$ J2000	$\delta$ J2000	$\sigma_\alpha^b$ arcsec	$\sigma_\delta^b$ arcsec	$\Theta^{(c)}$ arcmin	$C_t$ counts	$C_s$ counts	$C_m$ counts	$C_h$ counts	
3001	164704.14-454957.4	251.767277	-45.832630	0.06	0.06	1.6	38	0	11	27	
3002	164704.14-455100.2	251.767284	-45.850057	0.06	0.06	0.8	32	1	11	20	
3003	164704.15-455133.6	251.767302	-45.859349	0.05	0.05	0.6	47	0	13	34	
3004	164704.15-455118.1	251.767311	-45.855035	0.05	0.05	0.6	50	0	11	39	
3005	164704.16-455320.2	251.767343	-45.888959	0.09	0.10	1.9	14	1	5	8	
3006	164704.16-455002.9	251.767353	-45.834155	0.10	0.10	1.6	7	0	2	5	
3007	164704.16-455135.0	251.767366	-45.859734	0.06	0.06	0.6	19	0	5	14	
3008	164704.17-455010.5	251.767382	-45.836274	0.08	0.08	1.4	23	0	5	18	
3009	164704.18-455025.7	251.767450	-45.840474	0.06	0.05	1.2	36	1	13	22	
3010	164704.19-455126.4	251.767479	-45.857345	0.07	0.07	0.6	27	0	10	17	

Photometry

$C_{net,t}$ counts	$C_{net,s}$ counts	$C_{net,m}$ counts	$C_{net,h}$ counts	$E_{median}$ keV	$F_{photons,t}$ photons $cm^{-2} s^{-1}$	$F_{photons,s}$ photons $cm^{-2} s^{-1}$	$F_{photons,m}$ photons $cm^{-2} s^{-1}$	$F_{photons,h}$ photons $cm^{-2} s^{-1}$	$\log(P_{B,best})$
$25.9^{+7.2}_{-6.8}$	$-0.5^{+1.8}_{-2.3}$	$8.1^{+4.4}_{-3.2}$	$18.2^{+6.3}_{-5.1}$	3.22	$1.25 \times 10^{-7}$	NaN	$3.00 \times 10^{-8}$	$8.68 \times 10^{-8}$	-8.94
$12.9^{+6.8}_{-5.7}$	$0.7^{+0.8}_{-1.1}$	$3.7^{+3.4}_{-3.3}$	$8.4^{+5.1}_{-4.4}$	2.77	$6.97 \times 10^{-8}$	$2.32 \times 10^{-8}$	$1.50 \times 10^{-8}$	$4.49 \times 10^{-8}$	-2.23
$37.1^{+7.7}_{-8.8}$	$-0.1^{+1.8}_{-1.8}$	$8.9^{+4.7}_{-3.5}$	$28.2^{+6.9}_{-7.8}$	2.95	$2.19 \times 10^{-7}$	NaN	$3.93 \times 10^{-8}$	$1.65 \times 10^{-7}$	-15.2
$19.1^{+8.8}_{-7.2}$	$0.0^{+1.8}_{-1.8}$	$-0.1^{+3.5}_{-3.4}$	$19.2^{+7.8}_{-6.3}$	4.15	$8.95 \times 10^{-8}$	NaN	NaN	$8.85 \times 10^{-8}$	-5.1
$7.4^{+4.8}_{-3.7}$	$0.7^{+3.3}_{-1.8}$	$3.2^{+3.4}_{-2.6}$	$3.4^{+3.9}_{-2.7}$	2.02	$4.15 \times 10^{-8}$	$2.14 \times 10^{-8}$	$1.36 \times 10^{-8}$	$1.90 \times 10^{-8}$	-6.61
$3.1^{+2.5}_{-2.4}$	$-0.1^{+1.8}_{-1.8}$	$0.9^{+2.6}_{-1.4}$	$2.2^{+2.7}_{-1.4}$	2.24	$2.49 \times 10^{-8}$	NaN	$5.53 \times 10^{-9}$	$1.80 \times 10^{-8}$	-3.53
$9.7^{+5.4}_{-4.3}$	$-0.1^{+1.8}_{-1.8}$	$1.2^{+3.4}_{-2.1}$	$8.6^{+4.8}_{-3.7}$	3.46	$5.56 \times 10^{-8}$	NaN	$5.34 \times 10^{-9}$	$4.84 \times 10^{-8}$	-2.92
$11.1^{+5.9}_{-4.7}$	$-0.2^{+1.8}_{-1.8}$	$0.9^{+3.4}_{-2.1}$	$10.4^{+5.3}_{-4.2}$	4.99	$5.31 \times 10^{-8}$	NaN	$3.62 \times 10^{-9}$	$4.87 \times 10^{-8}$	-4.68
$19.4^{+7.1}_{-6.0}$	$0.6^{+0.8}_{-1.8}$	$7.2^{+4.7}_{-3.6}$	$11.6^{+5.8}_{-4.7}$	2.17	$1.06 \times 10^{-7}$	$2.04 \times 10^{-8}$	$2.94 \times 10^{-8}$	$6.27 \times 10^{-8}$	-3.70
$9.2^{+6.0}_{-5.2}$	$-0.5^{+1.8}_{-1.8}$	$3.7^{+3.8}_{-3.1}$	$6.0^{+5.2}_{-4.1}$	4.16	$4.66 \times 10^{-8}$	NaN	$1.44 \times 10^{-8}$	$2.98 \times 10^{-8}$	-2.60

Columns 1–11 are shown in the top table; columns 12–21 in the bottom table.

a: IAU designation.

b: single axis position error, representing only the random component of the position uncertainty.

c: Off-axis angle.

Photometric quantities are given in broad (*t*), soft (*s*), medium (*m*), and hard (*h*) bands.

$C_X$  indicate the total counts in the X band,  $C_{X,net}$  the net counts.

**Appendix B: EWOCs X-ray counterparts of the massive stars in Westerlund 1**

Table B.1 shows the EWOCs X-ray counterparts of the massive stars in Westerlund 1 listed in Clark et al. (2020).

**Table B.1.** Known massive stars in the EWOCs X-ray catalog

ID	Spectral type	Catalog name	C <sub>net,t</sub> counts	F <sub>photons,t</sub> photons cm <sup>-2</sup> s <sup>-1</sup>	Sep. arcsec
W9	sgB[e]	164704.13-455031.3	7975.3 <sup>8065.8</sup>	3.7×10 <sup>-5</sup>	0.2
W30	O4-5Ia	164704.10-455039.2	5930.2 <sup>7885.7</sup>	2.7×10 <sup>-5</sup>	0.2
W72	WN7b	164708.35-455045.4	5412.8 <sup>6008.4</sup>	4.5×10 <sup>-5</sup>	0.3
WRB	WN7o	164705.36-455104.8	3046.2 <sup>5852.8</sup>	1.4×10 <sup>-5</sup>	0.1
WRU	WN6o	164706.53-455039.1	1996.9 <sup>5487.5</sup>	9.6×10 <sup>-6</sup>	0.1
W44	WN9h	164704.19-455107.2	1221.9 <sup>5338.8</sup>	5.6×10 <sup>-6</sup>	0.3
W239	WC9d	164705.20-455225.0	903.2 <sup>3102.4</sup>	6.0×10 <sup>-6</sup>	0.0
W53	OBIa+OBIa	164700.38-455131.8	515.5 <sup>2990.6</sup>	2.5×10 <sup>-6</sup>	1.0
W36	OBIa+OBIa	164705.07-455055.2	514.7 <sup>2042.3</sup>	2.4×10 <sup>-6</sup>	0.4
WRO	WN6o	164707.65-455236.0	387.6 <sup>1952.0</sup>	2.5×10 <sup>-6</sup>	0.1
WRN	WC9d	164659.91-455525.6	375.2 <sup>1257.6</sup>	2.2×10 <sup>-6</sup>	0.4
W27	O7-8Ia <sup>+</sup>	164705.14-455041.4	340.1 <sup>933.7</sup>	1.5×10 <sup>-6</sup>	0.1
W13	B0.5Ia <sup>+</sup> +OB	164706.44-455026.1	258.0 <sup>873.0</sup>	1.2×10 <sup>-6</sup>	0.1
WRW	WN6h	164707.61-454922.1	243.0 <sup>558.7</sup>	1.3×10 <sup>-6</sup>	0.3
WRJ	WN5h	164702.47-455059.9	233.4 <sup>492.4</sup>	1.1×10 <sup>-6</sup>	0.1
W14c	WN5o	164706.09-455022.4	192.9 <sup>538.7</sup>	9.2×10 <sup>-7</sup>	0.3
W24	O9Iab	164702.15-455112.6	191.7 <sup>491.0</sup>	9.3×10 <sup>-7</sup>	0.2
W43c	O9Ib	164703.75-455058.5	188.5 <sup>407.7</sup>	1.0×10 <sup>-6</sup>	0.2
1041	O9.5Iab	164704.45-455109.4	170.4 <sup>367.7</sup>	7.9×10 <sup>-7</sup>	1.0
WRX	WN5o	164714.13-454832.0	154.2 <sup>395.2</sup>	8.6×10 <sup>-7</sup>	0.3
WRG	WN7o	164704.00-455125.1	146.8 <sup>355.3</sup>	6.8×10 <sup>-7</sup>	0.0
W50b	O9III	164701.21-455027.6	136.2 <sup>359.6</sup>	7.4×10 <sup>-7</sup>	1.0
W38	O9Iab	164702.88-455046.2	118.9 <sup>320.8</sup>	5.6×10 <sup>-7</sup>	0.3
W37	O9Ib	164706.01-455047.5	118.1 <sup>274.7</sup>	5.5×10 <sup>-7</sup>	0.1
W35	O9Iab	164704.20-455053.7	110.3 <sup>241.4</sup>	5.9×10 <sup>-7</sup>	0.2
W25	O9Iab	164705.77-455033.4	108.4 <sup>259.1</sup>	5.1×10 <sup>-7</sup>	0.1
W232	B0Iab	164701.43-455235.2	104.7 <sup>227.1</sup>	6.4×10 <sup>-7</sup>	0.4
W6a	B0.5Iab	164703.04-455023.7	98.5 <sup>249.5</sup>	4.6×10 <sup>-7</sup>	0.1
W17	O9Iab	164706.23-455049.3	96.7 <sup>217.5</sup>	4.8×10 <sup>-7</sup>	0.1
W74	O9.5Iab	164707.07-455013.0	93.7 <sup>207.8</sup>	4.9×10 <sup>-7</sup>	0.0
W15	O9Ib	164706.62-455029.6	92.1 <sup>178.1</sup>	4.5×10 <sup>-7</sup>	0.0
W47	O9.5Iab	164702.61-455117.8	89.0 <sup>206.4</sup>	4.4×10 <sup>-7</sup>	0.3
W57c	WN7o	164701.59-455145.2	88.9 <sup>177.2</sup>	5.3×10 <sup>-7</sup>	0.2
WRI	WN8o	164700.87-455120.6	86.6 <sup>203.3</sup>	4.0×10 <sup>-7</sup>	0.1
WRQ	WN6o	164655.54-455134.5	86.6 <sup>173.8</sup>	5.6×10 <sup>-7</sup>	0.4
1027	O9.5Iab	164701.02-455007.0	85.6 <sup>184.8</sup>	4.2×10 <sup>-7</sup>	0.7
1051	O9III	164706.98-454940.1	79.5 <sup>156.2</sup>	4.6×10 <sup>-7</sup>	0.2
1056	O9.5II	164708.69-455101.7	76.3 <sup>167.3</sup>	3.7×10 <sup>-7</sup>	0.6
W10	B0.5I+OB	164703.34-455034.6	75.8 <sup>141.3</sup>	3.5×10 <sup>-7</sup>	0.3
W8a	F8Ia+	164704.83-455025.5	73.7 <sup>159.9</sup>	3.4×10 <sup>-7</sup>	0.8
W1	O9.5Iab	164659.39-455046.7	69.8 <sup>133.8</sup>	3.4×10 <sup>-7</sup>	1.2
WRD	WN7o	164706.25-455126.4	69.3 <sup>148.4</sup>	3.1×10 <sup>-7</sup>	0.1
W62a	B0.5Ib	164702.52-455138.0	69.1 <sup>124.1</sup>	4.0×10 <sup>-7</sup>	0.2
W65	O9Ib	164703.88-455146.5	67.9 <sup>130.9</sup>	3.7×10 <sup>-7</sup>	0.2
WRV	WN8o	164703.79-455038.7	66.8 <sup>106.9</sup>	4.9×10 <sup>-7</sup>	0.1
1037	O9.5II	164702.84-455006.4	64.8 <sup>130.2</sup>	3.2×10 <sup>-7</sup>	0.1
W28	B2Ia	164704.66-455038.5	63.2 <sup>106.1</sup>	2.9×10 <sup>-7</sup>	0.1
W61b	O9.5Iab	164702.56-455141.9	61.3 <sup>122.3</sup>	3.1×10 <sup>-7</sup>	0.3
1030	O9.5Iab	164701.67-455258.0	60.1 <sup>98.5</sup>	3.4×10 <sup>-7</sup>	0.3
1040	O9-9.5I-III	164704.59-455008.1	59.9 <sup>120.1</sup>	4.0×10 <sup>-7</sup>	1.0

continued on next page

Table B.1.

ID	Spectral type	Catalog name	$C_{\text{net,t}}$ counts	$F_{\text{photons,t}}$ photons $\text{cm}^{-2} \text{s}^{-1}$	Sep. arcsec
1061	O9-9.5III	164709.61-455040.4	59.7 <sup>68.1</sup>	$3.1 \times 10^{-7}$	1.3
W84	O9.5Ib	164659.03-455028.3	57.0 <sup>64.8</sup>	$4.4 \times 10^{-7}$	0.1
1064	O9.5Iab	164711.50-455000.0	56.4 <sup>64.5</sup>	$2.9 \times 10^{-7}$	0.6
W241	WC9	164705.96-455208.3	56.3 <sup>64.3</sup>	$3.9 \times 10^{-7}$	0.9
1060	O9.5II	164709.19-455048.4	56.2 <sup>64.5</sup>	$2.8 \times 10^{-7}$	0.1
1036	O9.5Ia	164702.78-455212.7	55.8 <sup>63.8</sup>	$3.8 \times 10^{-7}$	0.3
1004	OeBe star	164653.44-455300.3	53.9 <sup>61.8</sup>	$2.7 \times 10^{-7}$	0.8
1058	O9III	164708.89-455124.5	53.7 <sup>61.6</sup>	$3.3 \times 10^{-7}$	0.1
W56b	O9.5Ib	164658.87-455145.9	52.5 <sup>60.1</sup>	$4.8 \times 10^{-7}$	0.2
W29	O9Ib	164704.40-455039.9	51.5 <sup>59.5</sup>	$3.7 \times 10^{-7}$	0.1
1023	O9III	164700.14-455110.3	49.7 <sup>57.8</sup>	$2.3 \times 10^{-7}$	1.0
W53	OBIa+OBIa	164700.55-455132.0	47.6 <sup>56.3</sup>	$2.3 \times 10^{-7}$	0.7
1034	O9.5Iab	164702.52-455148.3	47.4 <sup>55.3</sup>	$2.9 \times 10^{-7}$	0.1
1063	O9III	164710.74-454947.8	46.8 <sup>54.6</sup>	$2.3 \times 10^{-7}$	0.6
1005	B0Iab	164654.28-455154.8	43.8 <sup>51.3</sup>	$2.7 \times 10^{-7}$	0.4
1047	O9.5II	164706.12-455232.2	43.4 <sup>51.0</sup>	$2.9 \times 10^{-7}$	0.2
W41	O9Iab	164702.70-455057.1	43.0 <sup>50.8</sup>	$2.3 \times 10^{-7}$	0.2
1033	O9-9.5I-III	164702.37-455234.2	42.8 <sup>50.1</sup>	$2.7 \times 10^{-7}$	0.2
1018	O9.5Iab	164658.28-455057.0	41.8 <sup>49.1</sup>	$2.5 \times 10^{-7}$	0.4
W11	B2	164702.24-455046.8	41.4 <sup>49.2</sup>	$1.9 \times 10^{-7}$	0.2
1040	O9-9.5I-III	164704.54-455009.0	36.0 <sup>42.8</sup>	$2.4 \times 10^{-7}$	0.3
1038	O9III	164703.49-454857.1	34.8 <sup>41.9</sup>	$1.7 \times 10^{-7}$	1.1
1007	O9-9.5III	164654.90-455005.8	34.5 <sup>41.2</sup>	$2.1 \times 10^{-7}$	0.5
W243	LBV	164707.50-455229.0	33.7 <sup>40.4</sup>	$2.4 \times 10^{-7}$	0.7
1043	O9.5II-III	164704.56-455059.5	32.3 <sup>39.2</sup>	$2.2 \times 10^{-7}$	0.2
W86	O9.5Ib	164657.15-455010.0	30.3 <sup>36.5</sup>	$1.8 \times 10^{-7}$	0.1
W61a	B0.5Ia	164702.27-455141.7	28.6 <sup>35.6</sup>	$1.5 \times 10^{-7}$	0.2
W46b	O9.5Ib	164703.67-455120.5	28.5 <sup>36.2</sup>	$1.3 \times 10^{-7}$	0.9
1066	O9III	164712.60-455055.6	28.3 <sup>34.4</sup>	$2.0 \times 10^{-7}$	1.2
1050	O9.5II	164706.77-454955.2	26.4 <sup>32.6</sup>	$1.3 \times 10^{-7}$	0.0
WRH	WC9d	164704.23-455120.2	26.3 <sup>33.9</sup>	$1.2 \times 10^{-7}$	0.1
1029	O9-9.5III	164701.50-454950.1	25.5 <sup>31.6</sup>	$1.2 \times 10^{-7}$	0.6
W46a	B1Ia	164703.90-455119.9	24.5 <sup>32.4</sup>	$1.1 \times 10^{-7}$	0.4
W21	B0.5Ia	164701.10-455113.7	24.4 <sup>31.7</sup>	$1.1 \times 10^{-7}$	0.1
W5	WN10/B0.5Ia+WRS	164702.98-455018.5	23.7 <sup>29.7</sup>	$1.2 \times 10^{-7}$	1.0
1055	B0Ib(+O?)	164707.82-455147.1	23.1 <sup>28.8</sup>	$1.9 \times 10^{-7}$	1.2
W4	F3Ia+	164701.54-455037.1	22.3 <sup>28.6</sup>	$1.0 \times 10^{-7}$	1.3
1065	B0Ib	164711.60-454922.6	22.2 <sup>28.2</sup>	$1.1 \times 10^{-7}$	0.2
1048	B1.5	164706.28-455104.0	21.4 <sup>26.9</sup>	$1.7 \times 10^{-7}$	0.3
W34	B0Ia	164704.39-455047.3	21.3 <sup>29.4</sup>	$1.0 \times 10^{-7}$	0.1
W228b	O9Ib	164658.13-455301.2	21.1 <sup>26.5</sup>	$1.5 \times 10^{-7}$	0.9
1059	O9III?	164709.08-455320.7	21.1 <sup>26.4</sup>	$1.4 \times 10^{-7}$	0.3
W43c	O9Ib	164703.70-455057.7	21.0 <sup>27.0</sup>	$2.1 \times 10^{-7}$	0.8
1044	O9-9.5III	164705.56-454951.8	19.8 <sup>25.5</sup>	$1.0 \times 10^{-7}$	0.3
W43b	B1Ia	164703.52-455056.6	19.8 <sup>26.8</sup>	$1.1 \times 10^{-7}$	0.1
1059	O9III?	164709.11-455319.4	18.7 <sup>23.7</sup>	$1.4 \times 10^{-7}$	1.3
1042	O9.5II	164704.66-455206.8	17.9 <sup>23.3</sup>	$1.3 \times 10^{-7}$	1.1
W2a	B2Ia	164659.77-455051.8	17.3 <sup>22.8</sup>	$8.1 \times 10^{-8}$	0.9
1024	O9.5Iab	164700.78-455102.0	16.6 <sup>21.9</sup>	$8.6 \times 10^{-8}$	0.6
W50b	O9III	164701.11-455026.6	16.5 <sup>22.0</sup>	$8.7 \times 10^{-8}$	0.7
W228b	O9Ib	164658.02-455301.1	16.3 <sup>21.0</sup>	$1.2 \times 10^{-7}$	0.3
W243	LBV	164707.62-455228.4	15.9 <sup>21.1</sup>	$1.2 \times 10^{-7}$	0.7
W1	O9.5Iab	164659.20-455045.4	15.8 <sup>21.4</sup>	$7.9 \times 10^{-8}$	1.4
W4	F3Ia+	164701.35-455036.5	15.6 <sup>21.2</sup>	$7.4 \times 10^{-8}$	0.8
1032	O9-9.5III	164702.32-455017.1	15.3 <sup>20.7</sup>	$7.3 \times 10^{-8}$	0.7
1016	O9-9.5III	164658.09-455247.1	15.2 <sup>20.2</sup>	$8.2 \times 10^{-8}$	0.2

continued on next page



Table B.1.

ID	Spectral type	Catalog name	C <sub>net,t</sub> counts	F <sub>photons,t</sub> photons cm <sup>-2</sup> s <sup>-1</sup>	Sep. arcsec
W54	B0.5Iab	164703.14-455131.2	14.7 <sup>20.7</sup> <sub>9.30</sub>	6.9×10 <sup>-8</sup>	1.2
1014	O9-9.5III	164657.81-455119.3	14.4 <sup>19.3</sup> <sub>10.1</sub>	8.7×10 <sup>-8</sup>	0.4
1010	O+O?	164655.99-455210.1	14.4 <sup>19.2</sup> <sub>10.2</sub>	8.7×10 <sup>-8</sup>	0.7
1015	O9III	164657.97-455141.0	14.2 <sup>18.6</sup> <sub>10.3</sub>	1.5×10 <sup>-7</sup>	0.3
1049	B1-2Ia+	164706.66-454738.8	14.2 <sup>20.4</sup> <sub>8.4</sub>	8.5×10 <sup>-8</sup>	0.3
1031	O9III	164701.90-455056.1	14.0 <sup>18.6</sup> <sub>9.8</sub>	9.9×10 <sup>-8</sup>	0.2
1043	O9.5II-III	164704.63-455059.4	13.1 <sup>18.1</sup> <sub>8.6</sub>	1.2×10 <sup>-7</sup>	0.7
W23a	B2Ia+BI?	164702.56-455108.8	12.9 <sup>19.2</sup> <sub>7.1</sub>	6.0×10 <sup>-8</sup>	0.1
W63a	B0Iab	164703.41-455157.4	12.7 <sup>17.6</sup> <sub>8.3</sub>	9.0×10 <sup>-8</sup>	0.3
W55	B0Ia	164658.40-455131.1	12.5 <sup>17.0</sup> <sub>8.5</sub>	8.9×10 <sup>-8</sup>	0.0
1012	O9-9.5III	164656.95-455055.6	12.4 <sup>17.1</sup> <sub>8.3</sub>	7.1×10 <sup>-8</sup>	0.3
W238	B1Iab	164704.41-455227.7	12.1 <sup>17.1</sup> <sub>7.8</sub>	7.5×10 <sup>-8</sup>	0.1
1046	O+O?	164705.98-454955.4	11.6 <sup>16.6</sup> <sub>7.3</sub>	5.6×10 <sup>-8</sup>	1.4
1045	O9.5II	164705.83-455155.1	11.6 <sup>15.8</sup> <sub>8.0</sub>	1.0×10 <sup>-7</sup>	0.2
W75	M4Ia	164708.96-454958.7	11.6 <sup>16.4</sup> <sub>7.3</sub>	6.3×10 <sup>-8</sup>	0.4
1021	O9-9.5III	164658.77-455432.0	11.5 <sup>16.8</sup> <sub>6.8</sub>	6.2×10 <sup>-8</sup>	0.1
1013	O+O?	164657.54-455231.0	11.5 <sup>16.2</sup> <sub>7.4</sub>	6.4×10 <sup>-8</sup>	0.6
1035	O9-9.5III	164702.67-455151.2	11.3 <sup>16.1</sup> <sub>7.9</sub>	7.6×10 <sup>-8</sup>	0.4
1046	O+O?	164706.09-454957.7	11.1 <sup>15.9</sup> <sub>6.8</sub>	5.4×10 <sup>-8</sup>	1.3
1017	O9-9.5III	164658.24-455033.8	10.8 <sup>15.5</sup> <sub>6.7</sub>	6.0×10 <sup>-8</sup>	0.1
W20	M5Ia	164703.11-455218.9	8.8 <sup>13.3</sup> <sub>5.3</sub>	5.4×10 <sup>-8</sup>	0.3
1028	O9-9.5	164701.32-455137.5	8.7 <sup>13.6</sup> <sub>4.5</sub>	4.5×10 <sup>-8</sup>	0.6
1054	O9-9.5	164707.64-455141.1	8.0 <sup>11.7</sup> <sub>5.0</sub>	8.3×10 <sup>-8</sup>	0.3
W78	B1Ia	164701.48-454957.4	7.8 <sup>12.2</sup> <sub>4.0</sub>	3.8×10 <sup>-8</sup>	0.6
W373	B0Iab	164657.72-455320.0	7.7 <sup>11.9</sup> <sub>4.1</sub>	4.6×10 <sup>-8</sup>	0.1
1026	O9-9.5III	164701.01-454948.8	7.0 <sup>11.3</sup> <sub>3.3</sub>	3.5×10 <sup>-8</sup>	0.5
W71	B2.5Ia	164708.57-455049.8	5.5 <sup>9.4</sup> <sub>2.1</sub>	4.5×10 <sup>-8</sup>	1.5
1020	O9-9.5+O?	164658.49-455228.4	5.2 <sup>8.5</sup> <sub>2.5</sub>	3.7×10 <sup>-8</sup>	1.3
1008	O9.5II	164655.45-455154.2	5.1 <sup>8.7</sup> <sub>2.1</sub>	3.3×10 <sup>-8</sup>	0.1
1062	O+O?	164710.65-455047.2	5.0 <sup>8.7</sup> <sub>1.9</sub>	3.2×10 <sup>-8</sup>	0.9
1022	O9.5II	164659.88-455025.1	4.6 <sup>8.1</sup> <sub>1.6</sub>	3.0×10 <sup>-8</sup>	0.5
1045	O9.5II	164705.86-455154.2	4.4 <sup>7.5</sup> <sub>2.1</sub>	4.8×10 <sup>-8</sup>	0.8
W29	O9Ib	164704.47-455039.5	4.3 <sup>7.8</sup> <sub>1.4</sub>	4.8×10 <sup>-8</sup>	0.7

## Appendix C: Estimate of catalog completeness

The resulting completeness of our survey depends not only on the total exposure, but also on source crowding and the bright and irregular background. A full understanding of completeness will only be possible after the identification and classification of the OIR counterparts of the X-ray sources in order to distinguish between cluster members and sources in the foreground and background. However, we conducted some simple simulations using MARX, which, despite being based on strong assumptions, can provide some hints about completeness.

In order to simulate the cluster population, since the true shape of the IMF of Westerlund 1 is still a subject of debate, particularly in the low-mass regime, we made the assumption that the cluster IMF follows the law proposed by Kroupa (2001), which is applicable to most known young stellar clusters. We understand that the starburst environment can influence the distribution of stellar masses, leading to different mass functions. However, at this level of approximation, this is considered a secondary effect. To accommodate the compact morphology of the cluster, we assumed that cluster members are distributed according to a Gaussian function with a full width at half maximum of 4 arcminutes. Therefore, we did not account for the asymmetric morphology of Westerlund 1, as suggested by previous authors (e.g., Gennaro et al. 2011). Additionally, we assumed a total cluster mass of 45000 solar masses, encompassing stars with masses as low as 0.08 solar masses.

To convert the mass distribution into an  $L_X$  distribution, we utilized the  $L_X$  versus mass distribution derived from the *Chandra* Orion Ultradeep Project (COUP) conducted in the Orion Nebula Cluster (Preibisch & Feigelson 2005), accounting for its observed spread. We chose this distribution because the COUP survey provides the most complete X-ray observation of a young stellar cluster. However, it should be noted that this distribution may not accurately represent the population of Westerlund 1 due to differences in age and the presence of a distinct massive stellar population in this cluster. To account for this massive stellar population, we simply added the massive sources identified by Clark et al. (2005) with their corresponding measured  $L_X$  values to the simulated cluster population. Additionally, we normalized the COUP  $L_X$  versus mass distribution to account for the decline in stellar X-ray luminosity with age (Preibisch & Feigelson 2005), and we used the specified values for cluster distance and absorption to convert luminosity into flux.

We simulated a 1 Msec ACIS-I observation of this fake cluster, taking into account instrumental background<sup>14</sup>, and performed source detection using *Wavdetect* (thus not accounting for the source validation procedure we adopted with AE). By comparing the input and output lists of sources, we determined that the completeness in the 0.8-2 solar mass range is approximately 40% within the central 4 arcminute region, decreasing by approximately 10% in the inner 1 arcminute region. For more massive stars, the estimated completeness is around 85% regardless of the distance from the cluster center. It is important to note that this is a preliminary estimation of the completeness of the EWOCs X-ray catalog, which will be further validated through the identification of OIR counterparts and source classification.

<sup>14</sup> [https://cxc.harvard.edu/cal/Acis/detailed\\_info.html](https://cxc.harvard.edu/cal/Acis/detailed_info.html)